Journal of Sound and Vibration 630 (2026) 119701

Contents lists available at ScienceDirect

Journal of Sound and Vibration

journal homepage: www.elsevier.com/locate/jsvi

Part-span approximation of linear tone noise propagation in an aeroengine intake

Joseph S.P. Binns *, Long Wu, Alexander G. Wilson

Institute of Sound and Vibration Research, University of Southampton, Southampton, SO17 1BJ, UK

ARTICLE INFO

Keywords:
Noise
Aeroengine
Duct
Modal
Computation

ABSTRACT

A part-span methodology is proposed for the propagation of linear tone noise in aeroengine intake ducts. For fan rotor-associated tone noise sources in particular, but also rotor-stator interaction tones, much of the acoustic energy flux is concentrated towards the duct outer wall, offering the opportunity to reduce the computational expense of numerical predictions by neglecting low-span regions of the duct. Conventional computational fluid dynamics (CFD) methods can predict the acoustic field with reasonable accuracy but are too computationally expensive for iterative application during the design process. The methodology is investigated in four stages, starting with the impact on mode shape representation and in-duct propagation of individual Fourier-Bessel eigenmodes in a cylindrical duct through to far-field radiation. The approach is then applied to cases involving an axisymmetric, yet otherwise realistic, intake geometry, including a test case that considers steady flow distortion effects. Negligible errors for in-duct and far-field predictions are observed in many applied cases. Higher error levels are introduced for modes at low azimuthal harmonics and with ducts of high hub-tip ratios. In-duct, the error is closely linked to the amount of acoustic energy truncated in an approximated duct with an artificial hub wall and is associated with the redistribution of high-order radial mode components. Potential sources of error are identified and categorised: source truncation error, in-duct propagation error, and far-field radiation error. Computationally, the approximation can significantly reduce the size of the mesh required to resolve the acoustic field.

1. Introduction

Aircraft noise remains a significant challenge for the aviation industry with increasingly stringent legislation being enforced [1]. Contributions from the airframe and propulsion system amount to a complex noise profile which varies at different operating conditions. Certification points, approach, cutback, and sideline [2], are used by authorities to quantify noise impact on the environment and community, while cabin noise during cruise is also important for passenger comfort. The acoustic field in modern turbofan intakes is mainly comprised of upstream propagating noise from the fan system. At high-power operating points, rotor-associated tone noise sources are dominant.

For reasons primarily associated with increasing propulsive efficiency, but also related to noise reduction, the bypass ratio (BPR) of aeroengines has increased over time and will continue to in future Ultra-High Bypass Ratio (UHBR) designs [3]. To maintain reasonable weight and drag characteristics, engines are becoming more axially compact with non-dimensionally shorter intake regions upstream

* Corrresponding author.
E-mail addresses: J.Binns@soton.ac.uk (J.S.P. Binns), L.Wu@Soton.ac.uk (L. Wu), A.G.Wilson@soton.ac.uk (A.G. Wilson).

https://doi.org/10.1016/j.jsv.2026.119701
Received 28 May 2025; Received in revised form 14 January 2026; Accepted 6 February 2026
Available online 16 February 2026

of the fan. Consequently, the level of flow non-uniformity at the fan will increase which has been shown to complicate the noise profile and influence fan noise generation and intake propagation [4–16].

When the engine operates at high-power operating points, the tip speed of the fan blade can become supersonic, resulting in bow shocks at the leading edge and Prandtl-Meyer expansion fans forming across the rear surface of the blade [17]. The supersonic tip speed induces a rotor-locked cut-on acoustic pressure field, propagating non-linearly upstream through the intake duct. The shocks rotate with the fan (rotor-locked) and, according to weak shock theory, propagate through the duct at an undisturbed speed of sound relative to the oncoming flow [18]. For an ideal fan with identical blades, the pressure wave is consistent at every blade passage, resulting in discrete tonal noise at the Blade Passing Frequency (BPF) and its harmonics only. In reality, small geometric variations between blades, arising from manufacturing tolerances and wear, alter the acoustic profile. Variations in stagger angle, in particular, affect flow capacity and shock-detachment distance, influencing both shock strength and propagation angle [19]. These variations result in a pressure field that varies between blades and repeats every full rotation of the fan, producing tonal components at multiples of the fan rotational speed, known as Engine Order (EO) tones and commonly termed buzz-saw noise. When flow non-uniformities are introduced, the noise profile becomes even more complex. For example, acoustic energy from high-amplitude modal components can scatter into neighbouring modes during propagation due to interactions with inflow distortions, which are often described as low-order disturbances [12,20].

In academic and industrial communities, the application of computational methods that can accurately predict the acoustic field in an aeroengine intake is limited by the high expense of simulations. Hence, there is a requirement for more computationally efficient methods which still include significant effects on the propagation, such as three-dimensionality and non-linearity.

1.1. Predictions of fan tone noise generation and propagation

The Unsteady Reynolds-Averaged Navier Stokes (URANS) approach can reasonably account for most of the physics relevant to fan tone noise generation and intake propagation, including non-uniform flow, realistic geometries, shock formation and non-linear effects. Recent applications of the method have been used to simulate fan tone noise at various scales ranging from in-duct source characterisation, intake-fan configuration for upstream propagating noise, and whole nacelle-fan assembly, through to installed engine simulations. Doherty and Namgoong [9] validated the URANS method for noise predictions of installed turbofan intake geometries with 3D inflow effects. Daroukh et al. [14] demonstrated a similar method, including both upstream and downstream flow non-uniformities to predict the tonal noise generation and propagation in an aeroengine. This study highlighted the high computational expense of such simulations with a requirement of more than 1 million CPU hours, resolving only up to the second BPF. In recent years, the Lattice Boltzmann Method (LBM) has been applied to predict the acoustic field due to the fan stage of a turbofan engine [21,22]. Demonstrations have achieved reasonable predictions of broadband spectra at subsonic conditions and tonal components at transonic regimes. For tonal noise predictions, the computational demands of LBM are higher than those of other CFD methods, such as URANS, and may not be considered worthwhile. Alternatively, the full Euler formulation has been demonstrated for the prediction of aeroengine noise, also accounting for non-linear propagation effects close to the fan [23].

Linear computational approaches are often applied for predicting fan tone noise propagation according to linear assumptions, and are reviewed in detail by Astley et al. [24]. The frequency-domain Finite Element/Infinite Element (FE/IE) method is commonly used in computational aeroacoustics [11,25] and is based on a formulation derived from the Linearized Euler Equations (LEE), which reduces to the convected Helmholtz equation for uniform mean flow. It is effective for intake propagation and radiation predictions at frequencies of interest in large acoustic domains, but formulations relying on an acoustic velocity potential may be difficult to extend to strongly rotational flows. Goldstein's acoustic analogy for non-uniform mean flows [26] provides a more general theoretical framework that can account for shear and swirl effects, although its practical implementation remains challenging. The computational expense of FE/IE methods, which is memory limited, rapidly increases with problem size making large three-dimensional cases expensive [27]. In the time domain, structured high-order finite difference methods [28] and compact schemes [29] with Dispersion Relation Preserving (DRP) characteristics are commonly applied. The time-domain Discontinuous Galerkin Method (DGM) solves the Linearised Euler Equations (LEE) on unstructured grids, providing flexibility and computational efficiency [30]. Its high-order accuracy and adaptability to complex geometries make it suitable for aeroacoustic simulations in realistic configurations but it still relies on linear assumptions, making it inadequate for the non-linear propagation of high-amplitude fan tone noise in the intake. The non-linear region is generally limited to a portion of the intake but is significant for shock noise propagation. Adjustments to linear Computational Aeroacoustics (CAA) approaches can be made to partially account for non-linearity, such as those based on the analytical model introduced by Morfey and Fisher [17] and extended by Fisher et al. [31] and then in a series of studies from McAlpine and Fisher [18,32–35].

Eigen analysis methods have long been used to understand duct acoustic propagation. Tyler and Sofrin's [36] work on aeroengine tone noise is based on eigen analysis of uniform annular cylindrical ducts with uniform axial mean flow. Their work is still widely used to attain general estimates but has limitations making it insufficient in many cases. In realistic situations, aeroengine intake ducts are not uniform, flow is generally non-uniform radially (and in many cases azimuthally), and significant non-linear effects can often not be ignored. Rienstra [37] combined the eigenvalue approach with a multiple-scales methodology to accommodate annular cylindrical ducts of slowly varying radius. The Eigen Analysis in General Curvilinear Coordinates (EAGCC) method, introduced by Wilson [38], is an eigen analysis method for the propagation and modal decomposition of linear acoustic flow disturbances that can account for variations in mean flow as well as non-uniform, yet smoothly varying ducts and has been demonstrated for understanding the acoustic field in an aeroengine intake [39]. Eigen analysis methods are computationally faster than more conventional methods, such as a RANS CFD calculation, though are still generally limited by linear approximations. Wilson [40] successfully extended his

EAGCC model for two-dimensional non-linear propagation but highlighted the increased complexity of such predictions, indicating that further extension to three-dimensional flow/geometry would be significantly more laborious.

Alongside eigen analysis approaches, multimodal methods have been developed for tone propagation in aeroengine intake ducts. These methods describe the acoustic field as a superposition of eigenmodes with axially varying amplitudes, changes in duct shape, wall properties, or mean flow causing interactions between the modes. In this way, they retain the physical insight of modal analysis while extending applicability to ducts with curvature, lined walls, and mean flow. Early work focused on non-uniform ducts [41–43], with more recent developments broadening the framework to more realistic intake configurations [44–46].

For the radiation of noise to the far-field, various methods have been applied. Directly discretising and numerically solving the entire far-field domain is often neither practical nor feasible. Analytical approaches, such as integral formulations based on acoustic analogies, provide efficient alternatives. The porous Ffowcs-Williams and Hawkings (FWH) integral method [47], for example, has been widely used and demonstrated for intake noise radiation to the far-field [48]. For effective implementation, the control surface must be positioned away from significant flow disturbances and outside the non-linear region meaning that an extensive CFD solution may still be required. Numerical approaches, such as the Infinite Element (IE) method, are commonly used where the far-field domain is represented by a series of elements with infinite extent and acoustic waves are modelled as outwardly propagating solutions that satisfy the Sommerfeld radiation condition [49,50]. Analytical models, such as GXMunt [51], can also be applied for more simplified predictions of sound radiation from a semi-infinite, unflanged annular or circular duct and can be applied for intake noise radiation problems in the absence of mean flow. This model is further explained and implemented in Section 2.4.

1.2. Scope of the paper

The expense of computational methods that can accurately predict the complex, non-linear propagating acoustic field in an aeroengine intake duct, accounting for potentially significant three-dimensional flow and geometrical effects, is currently too high for iterative application in the design process.

Addressing this challenge, the current study proposes the ‘part-span approximation,’ a computational methodology designed to reduce the numerical cost of predicting tone noise in aeroengine intakes. At high-power operating points, much of the tonal acoustic energy flux in the intake is observed to be concentrated towards the outer walls of the duct. In response to this observation, the proposed part-span approximation neglects the low-span regions of the intake and resolves only from a given artificial hub wall up to the duct outer wall. For a uniform duct with uniform flow, this is equivalent to increasing the hub-tip ratio of the duct. In later applications, with non-uniform mean flow and geometry, a streamtube is used to define the artificial inner wall which has a specified hub-tip ratio at a given point near the acoustic source position. While primarily intended for application in non-linear computational approaches, this study investigates the feasibility of the part-span approximation for linear propagation of modal content in ducts. The objective is to evaluate its accuracy, identify potential sources of error, and inform its future application. A direct computational saving is achieved using the part-span methodology through the reduction in mesh size. An additional advantage is the avoidance of extremely small cells near the duct axis and around the spinner, which arise in fully-structured mesh approaches due to the high resolution required near the duct outer wall. For explicit time-domain solvers, the time step is constrained by the smallest cell size; thus, removing very small cells near the axis further improves efficiency and aids simulation convergence.

The scope of the present study is limited to fan tone noise up to the third blade passing frequency (3 BPF) of representative high-bypass-ratio turbofan engines propagating through the intake duct. As a result, the present study considers radial harmonics up to $n = 5$.

The part-span approximation is investigated in a series of steps. Firstly, the acoustic mode shape representation Section (2.1) and eigenvalues of modes in uniform ducts with uniform flow conditions Section (2.2) are considered for ducts with varying hub-tip ratios. Understanding is then extended to consider the propagation of modal content through uniform duct geometries with different hub-tip ratios Section (2.3), followed by analytical far-field radiation predictions Section (2.4). Finally, an application of the part-span approximation is demonstrated where the far-field radiation of modal content from an axisymmetric intake is calculated using a linear CAA method Section (3). A summary then collates the findings of the study and identifies the main causes of error which arise due to the approximation. Conclusions of the study are presented and potential areas of future work are outlined.

2. Part-span approximation of duct acoustic modes

Part-span approximation for a given duct introduces an artificial hub wall which, together with the outer wall of the original duct, forms an annular domain. The key parameter affecting the part-span approximation is the hub-tip ratio (ν) of the annular domain. The following section considers how acoustic modes in ducts are affected by varying the hub-tip ratio of the approximated part-span domain. The investigation follows four sequential parts which build understanding from fundamental modes in uniform ducts through to far-field predictions.

A. **Mode Shape Representation,** where analytical Bessel-Fourier modes are considered, independent of frequency, at a single axial position in a uniform duct.
B. **Effects on Axial Wavenumber - Amplitude and Phase Variation,** where (uniform) flow conditions and frequency variations are considered, focusing on the impact on axial wavenumbers.
C. **Linear In-duct Propagation,** where the first two subsections are unified and the propagation of mode profiles is considered in full and part-span domains.

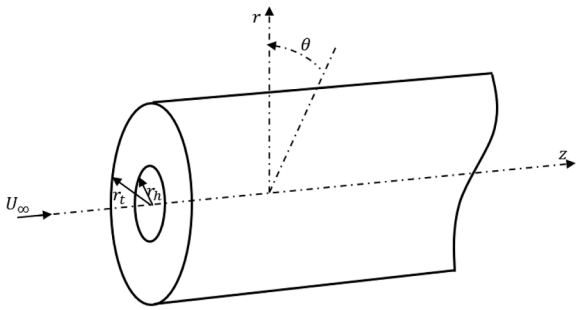

Fig. 1. Infinite, uniform annular duct geometry used for analytical consideration of mode shapes in ducts with different hub-tip ratios, $\nu = r_h/r_t$.

Table 1
Test matrix showing the range of variables considered throughout this section.

Azimuthal harmonic, m	$1 \rightarrow 72$
Radial harmonic, n	$1 \rightarrow 5$
Hub-tip ratio, ν	$0 \rightarrow 0.95$

D. Analytical Far-Field Radiation, where the far-field radiation of individual modes is considered from a semi-infinite unflanged duct of varying hub-tip ratios.

Fig. 1 illustrates the duct model used throughout this section. The duct is assumed to be hard-walled, axisymmetric and infinitely long in the axial (z) direction. The mean flow in the duct is uniform with only an axial velocity component of U_∞, and has no component radially or tangentially. In many cases throughout the following discussion, a baseline duct is used to consider the impact of a part-span approximation. Unless otherwise stated, the baseline duct is circular with no inner wall and a hub-tip ratio of $\nu = 0$.

2.1. Mode shape representation

The following section considers the impact of varying hub-tip ratios on the representation of acoustic mode shapes in a uniform duct. Table 1 highlights the different azimuthal and radial harmonics and the range of hub-tip ratios considered.

A range of modes were chosen to cover a wide range of applicable cases likely to be encountered in practice. For example, a typical fan in a turbofan engine may have around $B = 22$ blades, meaning the rotor-locked BPF mode will have an azimuthal harmonic order equal to the number of blades ($m = B$). Therefore, if one is interested in tonal content up to around the third BPF tone, the following test cases comfortably cover this range. In some applications, a range of radial modes can be axially cut-on meaning they will propagate and should be considered in noise predictions. Hence, up to five radial modes are considered in these tests. A range of hub-tip ratios up to ($\nu =$) 0.95 are considered. In many cases, it may be unreasonable to apply a part-span approximation with a hub-tip ratio this high, though the intention is to investigate the limits of the approximation.

Duct mode shapes can be described in terms of their azimuthal m and radial n harmonic indices, following, for instance, Rienstra [52]. The general radial profile is given by

$$\phi_{m,n}(r) = \alpha \mathrm{J}_m(\mu r) + \beta \mathrm{Y}_m(\mu r), \tag{1}$$

where α and β are scaling factors, and J_m and Y_m are Bessel functions of the first and second kind. The radial wavenumber μ can be computed according to the only non-trivial solution once a zero normal derivative boundary condition is applied at each wall (hard-wall boundary condition), giving

$$\mathrm{J}'_m(\hat{\mu}\nu)\mathrm{Y}'_m(\hat{\mu}) - \mathrm{J}'_m(\hat{\mu})\mathrm{Y}'_m(\hat{\mu}\nu) = 0, \tag{2}$$

where J'_m and Y'_m refer to the derivative of both Bessel functions with respect to r, $\hat{\mu}$ is the radial wavenumber non-dimensionalised by the tip radius ($\hat{\mu} = \mu r_t$) and ν is the hub-tip ratio ($\nu = r_h/r_t$). For any given circumferential harmonic m and hub-tip radius ν, Eq. (2) gives an infinite series of values of radial wavenumber $\hat{\mu}$, where each consecutive solution refers to subsequent radial mode orders.

Before the mode shape itself is considered according to Eq. 1, the variation in radial wavenumber values for different hub-tip ratios can be observed. For a range of circumferential harmonics between 1 and 72, Fig. 2 highlights the percentage difference in the computed radial wavenumbers using part-span domains of various hub-tip ratios when compared with the baseline value of a circular duct. When implementing the part-span approximation, an artificial wall is introduced at a given hub-tip ratio and hence the difference obtained in radial wavenumber can be considered an error with respect to the baseline case. The calculated percentage difference obtained for the first four radial wavenumber solutions is presented.

The red lines in Fig. 2 indicate the hub-tip ratio for each azimuthal harmonic which gives an error of 2% in the radial wavenumber value (compared to the value obtained for a circular duct). At the first radial harmonic ($n = 1$), the error is generally below 1%. As the hub-tip ratio increases for low circumferential harmonics, the error becomes more significant reaching up to around 40% in extreme

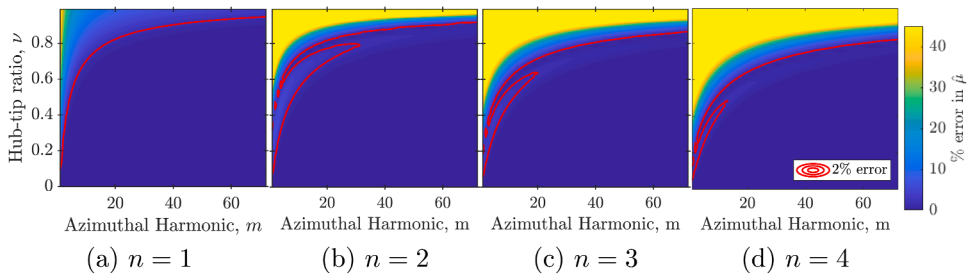

Fig. 2. Percentage error of computed radial wavenumber value for different duct hub-tip ratios, a range of circumferential harmonics from 1 to 72, and the first four radial harmonics. The red line (–) indicates the hub-tip ratio at which the percentage error when compared to a circular duct is at 2%. (For interpretation of the references to colour in this figure legend, the reader is referred to the web version of this article.)

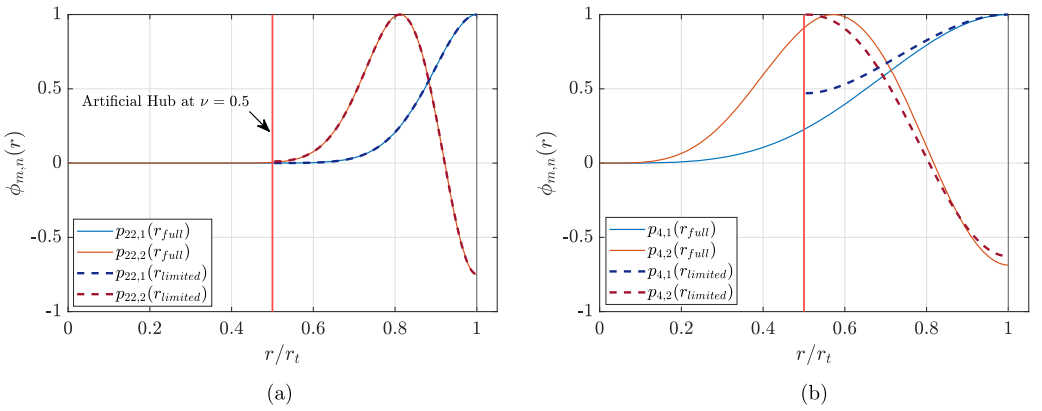

Fig. 3. The theoretical radial profile of duct mode shapes for two azimuthal and radial harmonics indices, computed for representative examples of full/circular (–) and limited (- -) annulus duct geometries. (a) Computed mode shapes for $m = 22$, $n = 1, 2$. (b) Computed mode shapes for $m = 4$, $n = 1, 2$.

cases. The same trend is observed for all subsequent radial wavenumber harmonics. In all cases, maximum error is obtained at low circumferential orders and high hub-tip ratios. The 2% error line is pushed to lower hub-tip ratios as radial harmonic increases. At higher circumferential harmonics, the error is still observed to be small for most hub-tip ratios.

For radial mode orders greater than one, a non-monotonic trend in error is observed. This arises from how the annular-duct eigenfunction compares with the baseline cylindrical-duct eigenfunction. The radial eigenvalue must satisfy both the hard-wall boundary conditions and the correct number of radial nodes (e.g., two for $n = 3$). As the hub-tip ratio increases, the inner wall can disrupt the mode shape, leading to error where either condition is no longer satisfied. The error can reduce again when the wall coincides with the first zero-derivative position of the cylindrical-duct mode, since the boundary condition is naturally satisfied while preserving the required number of nodes. Beyond this point, however, the full nodal structure can no longer be maintained, and the error increases monotonically.

The computed radial wavenumber ($\hat{\mu}$) values can be cast into Eq. (1) to obtain the general radial profile of each mode shape in the duct. Fig. 3 shows normalised computed mode shapes for circumferential mode numbers $m = 22$ (Fig. 3a) and $m = 4$ (Fig. 3b) at the first two radial harmonics ($n = 1, 2$) for a circular duct and a duct with hub-tip ratio of $\nu = 0.5$.

Fig. 3 highlights that at higher azimuthal orders, such as $m = 22$ (perhaps typical of a BPF tone), the variation in mode shape representation is visibly indistinguishable at both radial harmonics when comparing between a circular and limited annulus duct. At lower azimuthal harmonics (such as $m = 4$), the deviation is evident at both radial harmonic indices. For the $m = 4$, $n = 1$ case, the greatest deviation is towards the (artificial) hub and the difference becomes smaller at larger radii. Considering these mode shapes in isolation, the least deviation occurs when there is little signal energy below the artificial hub radius. As a result, the initial indication suggests that the impact of increasing the hub-tip ratio will be greatest for lower azimuthal order modes.

To further investigate, mode shapes are computed for a range of circumferential and radial harmonics and hub-tip ratios. The difference between mode shapes in circular and part-span domains is quantified to understand the potential error E in mode shape representation according to the ℓ_2 norm error which can be computed over the part-span region:

$$E = \frac{||\hat{\phi}_{m,n}(r) - \phi_{m,n}(r)||_2}{||\hat{\phi}_{m,n}(r)||_2}, \tag{3}$$

where $\hat{\phi}_{m,n}(r)$ refers to the pressure mode shape computed for the baseline circular duct and $\phi_{m,n}(r)$ is the mode shape computed for the part-span region of the duct.

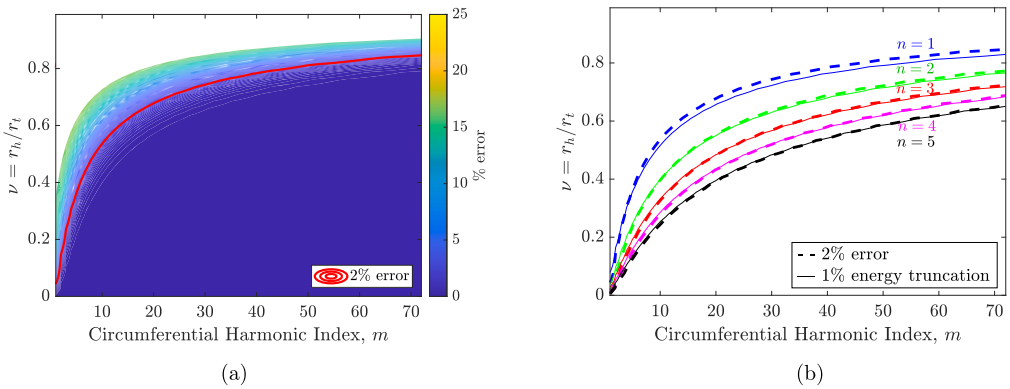

Fig. 4. Plots highlighting the percentage error introduced in mode shape representation, according to Eq. (3), by varying the duct hub-tip ratio for azimuthal harmonics ranging from 1 to 72. (a) Contour of percentage error in mode shape representation for a range of azimuthal harmonics at the first radial harmonic. The red line (–) highlights the point at which 2% error is introduced between the mode shapes in a circular duct and those in a duct with a given hub-tip ratio ν according to Eq. (3). The contour is truncated for modes where more than 20% of the acoustic energy is not represented in the part-span domain. (b) A plot highlighting the hub-tip ratio required to introduce a 2% error in mode shape representation (dashed line) for different radial harmonics. Also highlighted for the same respective radial harmonics is the hub-tip ratio at which 1% of the mode shape's acoustic energy is truncated (solid line). (For interpretation of the references to colour in this figure legend, the reader is referred to the web version of this article.)

Fig. 4 shows a contour plot of this error metric highlighting the relative difference in mode shape at different circumferential harmonics and hub-tip ratios. Fig. 4a shows the percentage error for modes at the first radial harmonic. The data is truncated based on the criterion that it is impractical to propose a part-span inner 'artificial' hub wall if more than 20% of the energy in the mode shape, i.e. $\int_r |\phi(r)|^2\, r\, \mathrm{d}r$, is not captured. Additionally, a red line highlights the hub-tip ratio where a 2% error arises compared to the mode shape in a circular duct. The error introduced is consistent with that observed by the radial wavenumber error plots, such that the greatest error is introduced for low circumferential harmonics and high hub-tip ratios.

Fig. 4a highlights that the energy truncation line follows a similar trend to the introduced error line. Fig. 4b compares, for the first five radial harmonics, the hub-tip ratio required to introduce 2% error in mode shape representation, with the hub-tip ratio that truncates 1% of the mode shapes' acoustic energy ($\int_r |\phi(r)|^2\, r\, \mathrm{d}r$). The two criteria align closely and suggest that the amount of error introduced is related to the amount of energy truncated.

It can also be observed in Fig. 4b that as the radial harmonic index increases, a lower hub-tip ratio is required to introduce the same level of error. For the first radial harmonic, a hub-tip ratio of 0.5 is sufficient to represent circumferential modes higher than order 10 within 2% error. Comparatively, at the fourth radial harmonic, the same hub-tip ratio (0.5) is only suitable for circumferential modes above order 15 according to the same criterion.

2.2. Effects on axial wavenumber - Amplitude and phase variation

The previous section covered how, independent of frequency and flow conditions, a part-span domain, parametrised by hub-tip ratio ν, can impact the representation of a mode shape in a duct for a range of azimuthal and radial harmonics, and hub-tip ratios. The following section begins to investigate potential propagation effects due to a part-span approximation, specifically looking at variations in the axial wavenumber k_z. To assist the following analysis, it is helpful to consider the application of a turbofan engine with a number of blades B, rotating at a shaft frequency Ω in a duct with axial mean flow at Mach number M. Table 2 highlights the variables considered in this section. A comprehensive range of azimuthal and radial harmonics and hub-tip ratios are covered in the previous section. Three in-duct Mach numbers are considered ranging from no flow ($M = 0$) through to a Mach number of $M = 0.6$. This high Mach number case is representative of the flow speed that may be present in an intake duct just upstream of the fan at high-power operating conditions. Three frequencies are considered and are specified in terms of the normalised free space wavenumber $\widehat{k_0}$ which is related to the rotational frequency ω by $\widehat{k_0} = (\omega/c_0)r_t$. The three chosen frequencies are representative of values similar to those at the blade passing frequency (BPF) and two of its harmonics (2BPF, 3BPF) for a typical turbofan engine operating in a transonic regime (supersonic tip speed).

The complex acoustic pressure in the duct at a single circumferential and radial harmonic can be described, following Rienstra [52],

$$p_{m,n}(r,\theta,z,t) = \phi_{m,n}(r)e^{-\mathrm{i}m\theta}e^{-ik_z z}e^{i\omega t}, \tag{4}$$

where θ is azimuthal position, z is axial position, t is time and ω is the rotating frequency of the modal pressure field. For rotor-locked noise, the rotational frequency ω depends on the shaft rotation frequency and the azimuthal harmonic such that $\omega = m\Omega$. The second exponential term, $\exp\{-ik_z z\}$, determines the phase and amplitude variation of the wave as it varies in axial position according to the axial wavenumber k_z. The subsequent analysis considers $\widehat{k_z}$, the non-dimensional axial wavenumber ($\widehat{k_z} = k_z r_t$), which is defined

Table 2
Test matrix highlighting the range of variables considered in the following section.

Azimuthal harmonic, m	$1 \rightarrow 72$
Radial harmonic, n	$1 \rightarrow 4$
Hub-tip ratio, ν	$0 \rightarrow 0.95$
Mach number, M	0, 0.3, 0.6
Frequency, $\widehat{k_0}$	24.0, 48.0, 72.0

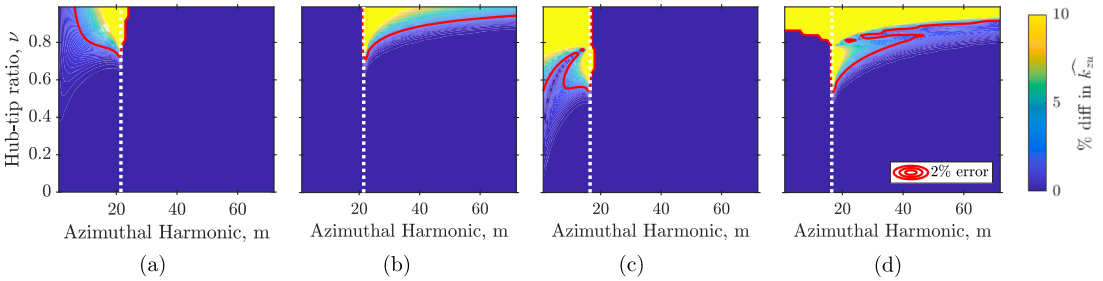

Fig. 5. Percentage difference in the real and imaginary part of the upstream axial wavenumber computed over a range of circumferential harmonics for different duct hub-tip ratios when compared to the absolute value obtained for a circular duct with $\widehat{k_0} = 24$ and $M = 0$. The red line (–) highlights the point at which 2% difference is introduced. The white dashed line shows the cut-on/cut-off boundary. (a) Real, $n = 1$. (b) Imaginary, $n = 1$. (c) Real, $n = 2$. (d) Imaginary, $n = 2$. (For interpretation of the references to colour in this figure legend, the reader is referred to the web version of this article.)

[52]

$$\widehat{k_z} = \frac{-M\widehat{k_0} \pm \sqrt{\widehat{k_0}^2 - \left(1 - M^2\right)\widehat{\mu}^2}}{1 - M^2}. \tag{5}$$

The radial wavenumber $\widehat{\mu}$ is dependent on the azimuthal and radial harmonic index and the hub-tip ratio, as has been previously discussed. For each given value of the radial wavenumber ($\widehat{\mu}$), two values for the axial wavenumber ($\widehat{k_z}$) are defined, referring to the upstream- and downstream-travelling waves. The axial wavenumber can be real or complex indicating whether the acoustic wave is cut-on or cut-off. For real values, the wave is said to be axially cut-on and propagates in the duct with constant amplitude. In comparison, for complex values, the wave is cut-off and decays exponentially. The rate of decay is dependent on the magnitude of the imaginary component of the wavenumber. This fact is significant when attempting to represent a mode in a part-span duct. For example, it may be sufficient to vary the radial position of the hub wall such that the errors in the cut-on modes are small, even if there are greater errors in cut-off modes.

The immediate concern in this analysis is the physical effect of different hub-tip ratios on the real and imaginary components of the axial wavenumber. It may be expected that if the baseline and part-span duct mode shapes appear similar, the difference in axial wavenumber will be small. In this instance, it is anticipated that the trends observed in the previous section will be repeated here.

Fig. 5 considers a zero flow case at the first frequency ($\widehat{k_0} = 24$), where the percentage difference in the real and imaginary parts of the calculated upstream axial wavenumber are presented over a range of circumferential harmonics and hub-tip ratios, and a circular duct is the baseline case. The first two radial modes are presented. Physically, a difference in the real component of the axial wavenumber will give rise to a phase error during propagation and a difference in the imaginary component will give rise to an amplitude error during propagation.

For first-order radial modes, which are cut-on in the datum circular duct, error is only observed in the real part of the axial wavenumber. For all cut-off modes in the circular duct, a difference in the imaginary part of the wavenumber is first observed. This suggests that for cut-off modes, the modal amplitude decay rate can be affected by the presence of a part-span approximation. In some cases and at very high hub-tip ratios, physically cut-off modes (those with an imaginary component) are observed to become cut-on. For example, at the frequency and flow conditions presented in Fig. 5, for an azimuthal harmonic of 22 (at the first radial harmonic), the circular duct mode is cut-off, while in a duct with hub-tip ratio of around 0.85 and above, this mode is cut-on.

Notably, a higher error is observed at the lowest hub-tip ratios for circumferential harmonics around the cut-off/cut-on boundary (which is highlighted by the white dashed line on the plot). This is illustrated by the red line on the figure highlighting the hub-tip ratio where 2% difference is computed.

For radial mode orders greater than one, modes that are otherwise cut-on can become cut-off when a part-span methodology is applied. As for any cut-on mode (including $n = 1$), at higher hub-tip ratios, an error is first introduced in the real part of the wavenumber. Then, for radial mode orders above one, continuing to increase the hub-tip ratio can cause the mode to transition to cut-off, which is illustrated by the difference observed in the imaginary part of the wavenumber (Fig. 5d). In the present study, the focus is on modes that are cut-off and subsequently become cut-on, since rotor-locked tones are of primary interest, and this cut-on to

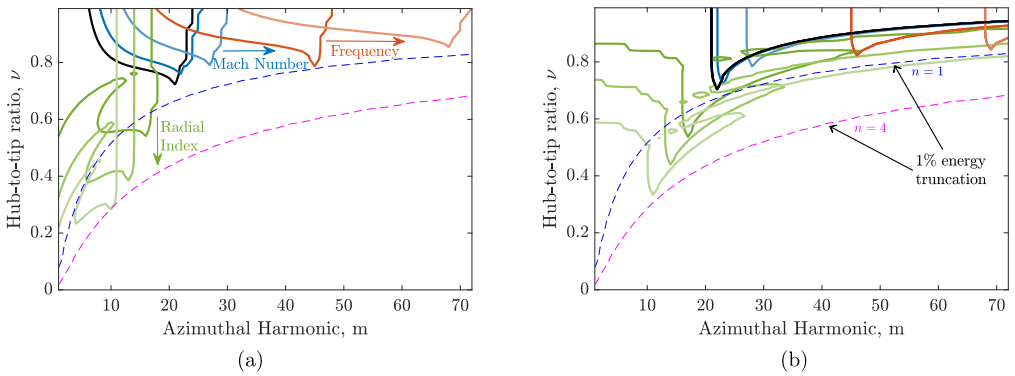

Fig. 6. Hub-tip ratio required to introduce a 2% difference in the real Fig. 6a and imaginary Fig. 6b components of the upstream axial wavenumber over a range of azimuthal harmonics. The baseline case is in black ($\widehat{k_0} = 24,\ M = 0,\ n = 1$). The orange lines indicate cases with increasing frequency ($\widehat{k_0} = 48,\ 72$), the blue lines indicate cases with increasing Mach number ($M = 0.3,\ 0.6$), and the green lines indicate cases of increasing radial harmonic ($n = 2,\ 3,\ 4$). For each case, only the interested parameter is varied, and other values remain as in the baseline case. Also highlighted with dashed lines (- -) is the hub-tip ratio at which 1% of the circular ducts mode shape energy for the first and fourth radial modes, as observed in Fig. 4b. (a) 2% difference in the real part of the upstream axial wavenumber. (b) 2% difference in the imaginary part of the upstream axial wavenumber. (For interpretation of the references to colour in this figure legend, the reader is referred to the web version of this article.)

cut-off effect is not observed for first-order radial modes. Nevertheless, this behaviour is noted to acknowledge the potential limitation of the part-span approach at high hub-tip ratios.

Fig. 6 considers how the impact on upstream axial wavenumber varies for different flow speeds, frequencies and radial harmonics. To demonstrate the impact, the hub-tip ratio at which a 2% error in axial wavenumber is achieved is plotted in Fig. 6 for a variety of parameter combinations. The baseline case (in black) is for zero flow, the first radial mode, and the lowest frequency considered ($\widehat{k_0} = 24$). As the duct Mach number is increased, two effects are observed. The first shows a shift to higher azimuthal harmonics (to achieve the same error). Furthermore, the hub-tip ratio required to achieve the same error level is pushed to higher values. A similar observation is shown as the frequency is increased and the impact is more significant. Also notable as frequency increases is the wider bandwidth of azimuthal harmonics which are impacted for higher frequencies. Nevertheless, these hub-tip ratios are reasonably high (> 0.75) and unlikely to be used for an applied case over a wide range of frequencies.

The primary effect due to an increase in radial index is a shift to lower azimuthal harmonics and hub-tip ratios to achieve the same error. Furthermore, for radial mode indices greater than one, the pattern of hub-tip ratio to achieve the same level of error is more complex than previously observed. The hub-tip ratios required to achieve a significant error are also relatively low, meaning this could be a constraint for some applications. The impact of varying Mach number and frequency on higher radial index modes follows the same trend as that observed for the first radial index.

Also highlighted on Fig. 6 with a dashed line is the hub-tip ratio required to truncate 1% of the energy in the mode shapes of both the first and fourth radial modes, as introduced in Fig. 4b, where this value is shown for the first five radial indices. As similarly observed in the previous section, to ensure less than 2% error is introduced, one should ensure that no more than 1% of the energy in the mode shape is truncated. Hence, this can be considered a reasonable estimate to ensure low error in an applied situation.

Fig. 6 suggests that, as well as taking care close to the cut-off/cut-on boundary, when the objective is to consider high-order radial modes at low circumferential harmonics, a significant error can be introduced for ducts with relatively low hub-tip ratios. This is unlikely to be a significant issue in many applied cases, such as the rotor-alone case, as high azimuthal harmonics generally have few radial modes cut-on (in many cases, only one). It was also shown that for modes well cut-on (or well cut-off), reasonably high hub-tip ratios were required to introduce significant differences in the computed axial wavenumbers. This is particularly the case for the first radial mode order and for higher azimuthal harmonics.

2.3. Linear in-duct propagation

Both static mode shape and propagation effects have been discussed separately. The following analysis unifies these effects by considering the linear propagation of modes through uniform ducts of different hub-tip ratios and with a uniform mean flow. Table 3 presents the test matrix for the following investigation. For each test, the baseline duct hub-tip ratio is $\nu = 0.2$ which is typical of the plane immediately upstream of a fan in a high bypass ratio turbofan engine. A Mach number of $M = 0.6$ is chosen for all cases and all baseline duct modes consider only the first radial harmonic. The three cases are chosen to show the impact of a part-span approximation on the in-duct propagation of mid- and low-order azimuthal harmonics. In the first two cases, the mode is cut-on in the baseline duct, while in the third case, the mode is cut-off. To evaluate the effect of propagating a source through a part-span domain (with $\nu > 0.2$), the baseline mode is truncated at the source plane, decomposed into its radial harmonic components through a Bessel breakdown and propagated upstream. Following the propagation of each radial component, the radial profile of acoustic pressure can be reconstructed and compared with that calculated in the full-span duct. It can also be useful to consider the amplitude of each propagated radial component individually, which is later discussed.

Table 3
Test matrix. [1]Represents the baseline hub-tip ratio in each test case.

Frequency, $\widehat{k_0}$	Azimuthal harmonic, m	Radial harmonic, n	Hub-tip ratio, ν	Mach number
5	4	1	0.2[1]	0.6
			0.5	
14	11		0.2[1]	
			0.5	
3.3	4		0.2[1]	
			0.75	
22	22		0.2[1]	
			0.5	
16.5	11		0.2[1]	
			0.5	
11	6		0.2[1]	
			0.5	

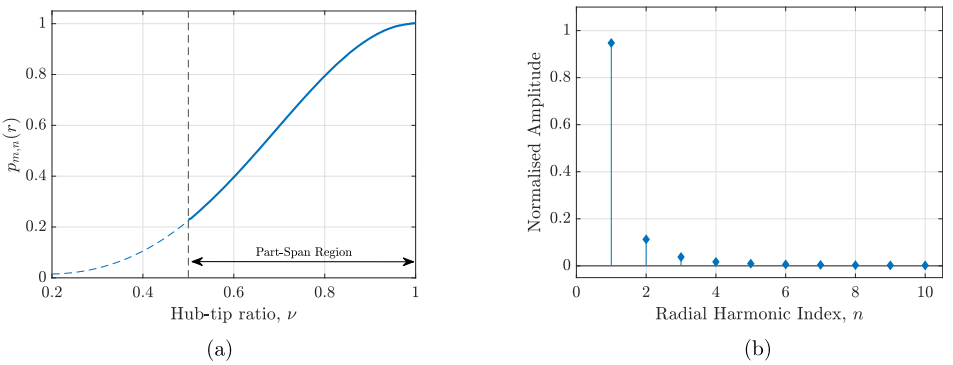

Fig. 7. Source plane ($z = 0$) pressure profile (Fig. 7a) decomposed into its radial harmonic indices in the part-span domain (Fig. 7b) for an annular duct mode with uniform mean flow at Mach number 0.6 and frequency of $\widehat{k_0} = 5$. (a) The acoustic pressure profile of a cut-on $m = 4$, $n = 1$ mode in a full domain ($\nu = 0.2$) and part-span domain ($\nu = 0.5$) at the source plane ($z = 0$). (b) The amplitudes of each radial harmonic index of the truncated pressure profile in the part-span (solid line) following a Fourier-Bessel decomposition at the source plane ($z = 0$).

Consider an $m = 4$, $n = 1$ mode in a uniform annular duct with a uniform mean flow at Mach number 0.6 and frequency of $\widehat{k_0} = 5$ which is cut-on with a real upstream axial wavenumber $\widehat{k_{zu}} \sim -5$. This mode is truncated in a part-span domain at a hub-tip ratio of 0.5. A Bessel decomposition of the truncated mode shape is applied to derive the amplitude coefficients A_n of each radial harmonic n. Fig. 7a shows the acoustic pressure profile of the mode at the source plane ($z = 0$) in the part-span region. While the full domain pressure profile has only contributions from the first radial harmonic index, a decomposition of the part-span profile, shown in Fig. 7b, highlights the mode scattering effect into higher radial harmonics. This effect occurs before any propagation of the profile and is highlighted as a source truncation error, that is, an error introduced at the source plane due to the truncation of the domain.

Following this decomposition, the amplitude of each respective radial harmonic can be attained at any axial position according to

$$A_{n,\text{prop}} = A_n e^{-ik_z z}, \tag{6}$$

where the axial wavenumber is dependent on the radial harmonic index. For this case, the first radial harmonic index is cut-on, and all subsequent ones are cut-off meaning only the first will propagate while the others will decay at a rate dependent on the imaginary component of the axial wavenumber. Fig. 8b shows the coefficients of each radial harmonic index for the pressure profile after being propagated upstream by a distance of 1 radius ($z = -r_t$).

This plot highlights that, following propagation, only the first radial component comprises the resultant profile and higher indices have decayed. As a result, the propagated profile deviates from that in the full domain, as shown in Fig. 8a. The error introduced here is done so during the initial period of propagation as the high-order radial components decay. Once they have decayed, the difference between the mode shapes will remain constant as is later shown. For this reason, this error is also classed as a source truncation error. In this case, however, another error is introduced during propagation and is classed in this study as an in-duct propagation error. While only the first radial harmonic is cut-on, the presence of the part-span hub wall has altered the axial wavenumber of this mode. As a result, this in-duct propagation error results in a bulk phase difference as the mode axially propagates in the duct.

For a higher circumferential harmonic, such as $m = 11$ with a frequency $\widehat{k_0} = 14$, and which is well cut-on in the same duct, the same analysis can be completed. Fig. 9 presents the propagated mode shapes in the datum and part-span domains. It can be seen how the deviation between the part-span and full-span propagated pressure profiles is minimal. The only notable difference is at the inner wall of the part-span domain, where the hard-walled boundary condition must be satisfied. Once again, the presence of the part-span

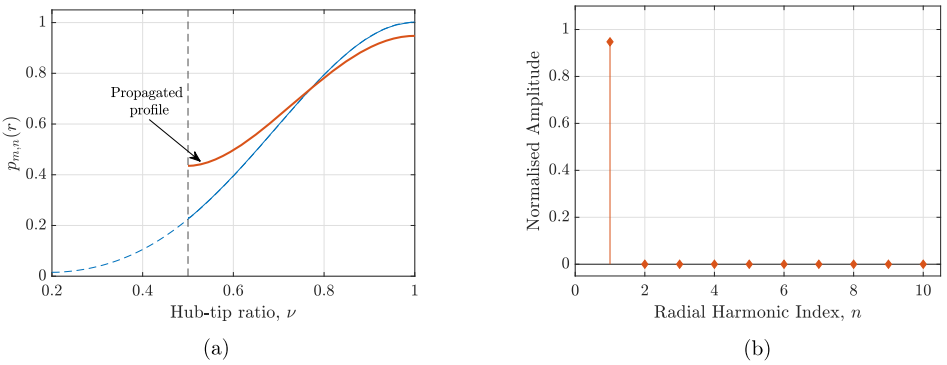

Fig. 8. Propagated acoustic pressure profiles for full (blue) and part-span (orange) domains and the decomposition of the propagated part-span pressure profile for the source in Fig. 7. (a) The acoustic pressure profile after propagating the profile in Fig. 7a by an upstream distance of 1 duct radius ($z = -r_t$). (b) Fourier-Bessel decomposition of the propagated profile in Fig. 8a into its radial harmonics. (For interpretation of the references to colour in this figure legend, the reader is referred to the web version of this article.)

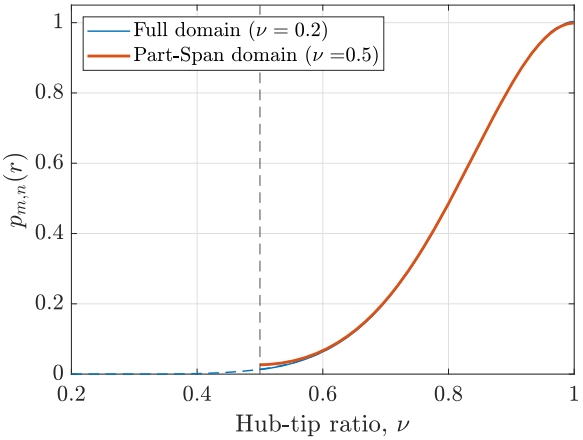

Fig. 9. The pressure profiles of an $m = 11$, $n = 1$, well cut-on mode with a Mach number of 0.6 and frequency of $\widehat{k_0} = 14$ after propagation upstream by a distance of 1 duct radius ($z = -r_t$) in a full (blue) and part-span (orange) domain. (For interpretation of the references to colour in this figure legend, the reader is referred to the web version of this article.)

domain will also introduce a bulk (that is, radially uniform) phase error due to the difference in axial wavenumbers. For this case, that difference is only small as the part-span boundary intersects the profile at a point of low amplitude.

The previous two cases considered a full domain mode which had a cut-on axial wavenumber. The analysis in Section 2.2 showed that for some cases, a physically cut-off mode could become artificially cut-on when a part-span approximation is applied. To investigate a case like this, an $m = 4$, $n = 1$ acoustic mode with a complex upstream axial wavenumber ($\widehat{k_{zu}} \sim 2 + 2i$) in the full domain is used as the source in a part-span domain with $\nu = 0.75$. At the source plane, the acoustic pressure profiles are shown in Fig. 10a as well as the respective coefficients of each radial harmonic which are plotted in Fig. 10b.

While the upstream axial wavenumber is complex in the full domain (for $m = 4$, $n = 1$), for the part-span domain, the axial wavenumber of the first radial harmonic is entirely real. Consequently, as shown in Fig. 11a, the propagated pressure profiles vary significantly between the full- and part-span domains due to the error introduced at the source plane. This error arises from the axial wavenumber changing from a complex to a real value due to the change in duct hub-tip ratio. Since it is introduced at the source plane and does not evolve during propagation, it is classified as a source-truncation error. For the full domain propagated pressure profile, the amplitude has decayed through the duct to a low amplitude, while for the profile propagated in the part-span domain, the amplitude is still high. This is due to the part-span domain modifying the upstream axial wavenumber of the first radial harmonic such that it becomes artificially cut-on. It is noted that only the first radial harmonic axial wavenumber is wholly real. While this is an extreme case, with an input mode close to the cut-on boundary and a high hub-tip ratio, a situation like this highlights a potential limitation of the part-span approximation. However, it is noted that any mode of this type lies close to the cut-off boundary, and hence carries relatively little acoustic power. Thus, while the error of in-duct pressure level may be large, the error in the far-field can be much smaller.

The previous three cases presented have considered two discrete axial positions: the source plane and an axial position one radius upstream of the source. The amplitude of different radial harmonic coefficients A_n can be considered at increasing axial distance $|z|$.

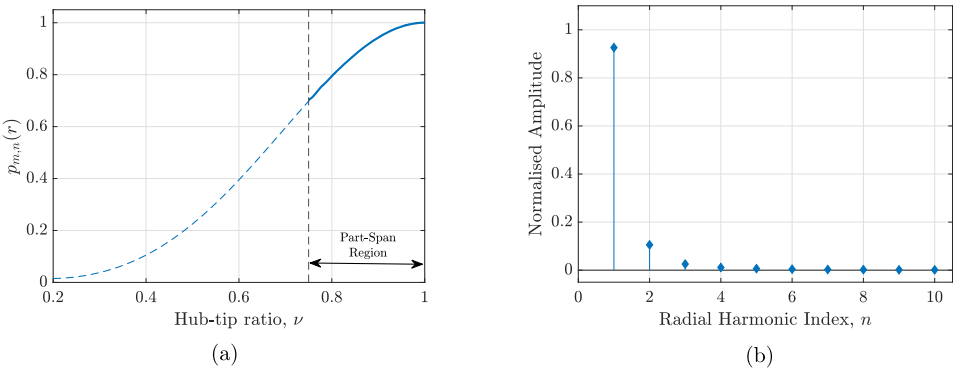

Fig. 10. Source plane ($z = 0$) pressure profile (Fig. 10a) decomposed into its radial harmonic indices in the part-span domain (Fig. 10b) for an annular duct mode with uniform mean flow at Mach number 0.6 and frequency of $\widehat{k}_0 = 3$. (a) The acoustic pressure profile of a $m = 4$, $n = 1$ mode in a full domain ($\nu = 0.2$) and part-span domain ($\nu = 0.75$) at the source plane ($z = 0$) which is cut-off in the full domain and becomes cut-on in the part-span domain. (b) The amplitudes of each radial harmonic index of the truncated pressure profile in the part-span domain following a Fourier-Bessel decomposition at the source plane ($z = 0$).

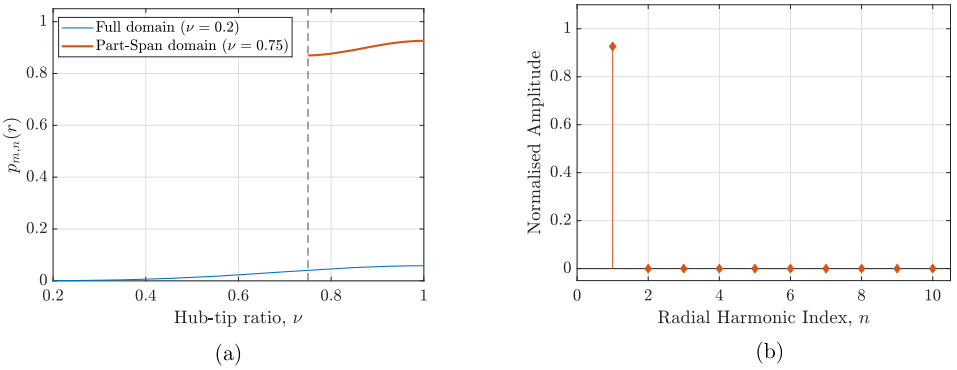

Fig. 11. Propagated acoustic pressure profiles for full (blue) and part-span (orange) domains and the decomposition of the propagated part-span pressure profile for a source which is cut-off in the full domain and cut-on in the part-span domain. (a) The acoustic pressure profile after propagating the profile in Fig. 10a by an upstream distance of 1 duct radius ($z = -r$). (b) Fourier-Bessel decomposition of the propagated profile in Fig. 10b into its radial harmonics. (For interpretation of the references to colour in this figure legend, the reader is referred to the web version of this article.)

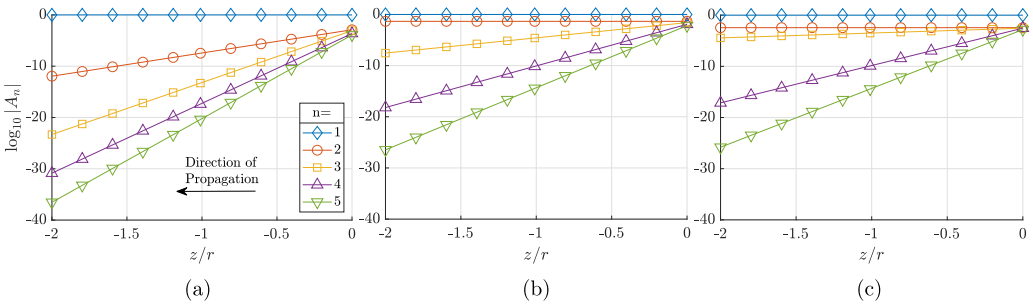

Fig. 12. The amplitude $\log_{10}|A_n|$, plotted against axial distance (normalised by the duct outer wall radius), of the first 5 radial modes of three different input signals for a part-span domain with $\nu = 0.5$ and a uniform axial flow of $M = 0.6$. (a) $m = 22$, $\widehat{k}_0 = 22$. (b) $m = 11$, $\widehat{k}_0 = 16.5$. (c) $m = 6$, $\widehat{k}_0 = 11$.

For an upstream travelling mode in a duct with an axial mean flow of $M = 0.6$ and a hub-tip ratio equalling 0.5, the amplitude of the first five radial orders is shown for three different azimuthal harmonic indices ($m = 22, 11, 6$, $n = 1$) and frequencies in Fig. 12. These cases were chosen to include a situation in which, as is shown in Fig. 12b and c, the state of the second radial mode becomes cut-on in the part-span domain. For all cases, in the full-span (datum) duct, only the first radial mode, which is cut-on, is present and propagates through the propagation region.

To further investigate this, the difference between pressure profiles propagated in domains of different hub-tip ratios is quantified using an area-weighted mean square-based error metric E. A simple mean square pressure difference would be misleading in this

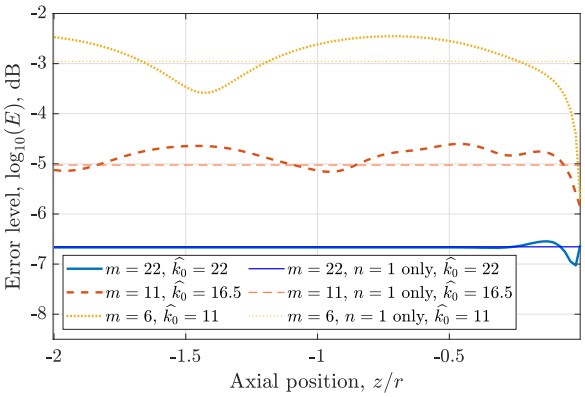

Fig. 13. The modified mean square error, corrected for constant phase deviation, between pressure profiles in a datum duct ($\nu = 0.2$) and a part-span duct ($\nu = 0.5$) calculated as both are linearly propagated through the respective ducts and evaluated in the part-span region. Also highlighted is the error value when only the first-order radial mode is propagated in the part-span duct for each case.

case because the change in axial wavenumber can introduce a bulk phase shift, as discussed earlier in this section. Over the length of the intake duct, this can generate a very large error even if only a single mode is cut-on (illustrated in Appendix A), even though in this case, a bulk phase shift has no effect on far-field amplitude or directivity.

For this reason, a modified mean square-based error metric is used where a radially uniform phase shift is added to the solution in such a way as to minimise the calculated error. The procedure for doing this is shown in Appendix A and results in the following equation

$$E = \min_{\theta} \left(\frac{\int |pe^{i\theta} - \hat{p}|^2 r \, dr}{\int r \, dr} \right) \tag{7}$$

where p is the profile propagated in a part-span domain and $\hat{p}$ is the profile propagated in the datum case.

In this way, radially varying phase errors stemming from multiple modes that affect far-field amplitude and directivity are accounted for in the error metric, whereas bulk (radially uniform) phase shifts are neglected.

For the three cases presented in Fig. 12, this error is plotted across an axial propagation distance of 2 duct radii in Fig. 13.

For the $m = 22$, $\widehat{k_0} = 22$ case, the error is relatively low. Close to the source, there is some variation in the error as lower amplitudes of higher radial order modes $n > 1$ (which are cut-off) decay. The error can be categorised as a source truncation error, as after the initial propagation, the error remains constant. Phase variations introduced by difference in axial wavenumber are intentionally excluded by the error metric definition.

In comparison, for the other two cases, where the second radial mode becomes cut-on, as is shown in Fig. 12b and c, the error quickly increases close to the source plane and gradually oscillates across the propagation region at a higher level. For the lowest azimuthal order case ($m = 6$), the calculated error is relatively high. The error arises from the combined effect of the cut-on second radial mode and the weakly cut-off third mode, which retains significant amplitude throughout the propagation region. The axial oscillations result from interference between cut-on and weakly cut-off modes with appreciable amplitude, as observed for the low-m cases. As a result, this type of error is categorised as an in-duct propagation error.

In practice, it may be possible to mitigate the in-duct propagation error introduced by the methodology. One possible strategy is to retain only the original mode order in the part-span case, even when higher radial modes become cut-on in the part-span domain. For instance, as illustrated in Fig. 13, when only the first-order radial mode is propagated in the part-span domain, the modified error metric remains constant along the propagation region. This highlights that the only apparent error stems from changes in both the shape and the amplitude of the first-order radial mode between domains, due to source truncation.

In the following analysis, an amplitude correction (described in detail in the next section) is applied to compensate for the amplitude discrepancy between the full- and part-span cases, based on the acoustic power of the incident mode in each configuration.

2.4. Analytical far-field radiation

Following consideration of the in-duct acoustic field, attention is now turned to the impact of a part-span approximation on far-field radiation. This is investigated using the analytic far-field method GXMunt, as presented by Gabard and Astley [51] in 2006. It is a theoretical framework that can predict noise propagation from turbofan engine ducts and radiation of sound waves into the far-field. It has been typically applied for aft-noise prediction from annular ducts and assumes an infinite duct centre body. Hence, it is a suitable method to investigate the impact of a centre body on far-field noise predictions. It has also been demonstrated for upstream-radiating noise from turbofan engines but neglects mean flow effects.

For the following predictions, the radiation of intake noise to the far field is considered. The analysis is performed without applying any near-field approximations, and the far-field directivity function, $D_p(\varphi)$, is computed for each configuration. The resulting far-field

Table 4
Test matrix highlighting the combination of variables considered in the following far-field predictions.

Azimuthal harmonic, m	Radial harmonic, n	Frequency, $\widehat{k_0}$	Mach number, M	Hub-tip ratio, ν
22	1	25	0	0, 0.2, 0.5, 0.75
11		14		
6		8		

acoustic pressure distribution is then obtained as

$$p(R,\varphi) = \frac{1}{R} D_p(\varphi), \tag{8}$$

where R is the distance to the far-field observation point and φ is the polar angle measured from the upstream engine axis. Table 4 summarises the test matrix used for the present far-field predictions. Four hub-tip ratios are considered, ranging from a cylindrical duct ($\nu = 0$) to an annular duct with $\nu = 0.75$. Three azimuthal harmonics, $m = 6, 11$, and 22, are examined at corresponding frequencies of $\widehat{k_0} = 8$, 14, and 25. In all cases, only a single radial harmonic is cut-on. These input parameters were selected to be representative of conditions similar to those observed for rotor-locked tones, and as a result, tonal frequency scales with azimuthal mode order.

To provide a reasonable comparison between cases, the far-field results are scaled such that the upstream-travelling acoustic wave at the source plane carries the same acoustic energy flux in each configuration, regardless of hub-tip ratio [51]. This scaling allows the influence of duct geometry on far-field directivity to be isolated from differences in acoustic energy flux at the source position (in the duct). The approach is formulated for general use with the part-span approximation and therefore includes uniform mean-flow effects, although no mean flow is considered in the present analytical far-field radiation study. The instantaneous acoustic intensity with mean flow is given by [53]

$$I = (p' + \rho_0 u' u_0)(u' + \frac{p'}{\gamma p_0} u_0), \tag{9}$$

where p' and u' are fluctuations of the static pressure and velocity; ρ_0, p_0 and u_0 are the time-averaged values of the flow density, static pressure and velocity; and γ is the ratio of specific heats for an ideal gas. The acoustic power is established by integrating the time-averaged acoustic intensity over the surface S,

$$P = \int_S \langle I \rangle \, \mathrm{d}S. \tag{10}$$

In the present case, only cut-on, isolated upstream travelling acoustic modes are considered. As a result, it is possible to show that the acoustic power is given by

$$P = \frac{1}{2} \rho_0 c_0 k_0^2 \, \eta_{mn} |C_{mn}^-|^2 \int_\theta \int_r |\phi_{mn}(r)|^2 r \, \mathrm{d}r \, d\theta, \tag{11}$$

where C_{mn}^- is the complex mode amplitude of the velocity potential for a given upstream travelling mode, η_{mn} is given by $\eta_{mn} = \sqrt{1 - (1 - M^2)\mu_{mn}^2 / k_0^2}$ (and is entirely real for a cut-on mode). Since the current application is to compare the energy of the incident mode in full- and part-span ducts, a correction factor δ, in dB, can be defined

$$\delta = 10 \log_{10} \left(\frac{\widetilde{P_{full}}}{\widetilde{P_{part}}} \right), \tag{12}$$

where

$$\widetilde{P_{full}} = \eta_{mn,full} |C_{mn,full}^-|^2 \int_{r_0}^{r_1} |\phi_{mn,full}(r)|^2 \, r \, \mathrm{d}r, \tag{13}$$

and

$$\widetilde{P_{part}} = \eta_{mn,part} |C_{mn,part}^-|^2 \int_{r_{0,part}}^{r_1} |\phi_{mn,part}(r)|^2 \, r \, \mathrm{d}r, \tag{14}$$

provided that the modes considered in each duct have the same radial and azimuthal orders, and frequency, as is the case in the present study.

Furthermore, as only a single radial mode is cut-on in all configurations (different hub-tip ratios) for each case, the source for each prediction contains only the original azimuthal and radial ($n = 1$) mode order and no contribution from high order radial modes (even if they have initial amplitude when they are truncated) as they are cut-off and will not propagate, nor radiate to the far-field (using the current method). As a result, the 'equivalent' source is a single mode with the same mode indices, and includes an amplitude correction, as highlighted above.

Fig. 14 presents the far-field radiation patterns. Initial observations highlight that the far-field pressure observed for the highest azimuthal mode considered ($m = 22$) is most consistent across all hub-tip ratios plotted. For this azimuthal mode, the only variation is observed at the highest hub-tip ratio ($\nu =$) 0.75. In this case, the peak amplitude is around 0.5 dB higher in this extreme hub-tip ratio case compared to the circular duct.

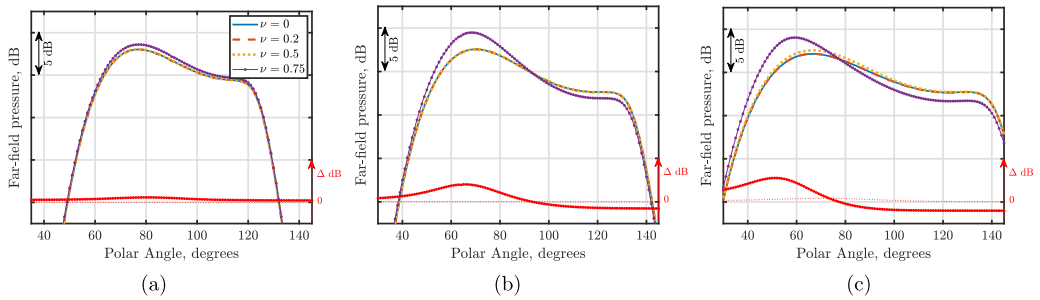

Fig. 14. Far field pressure predictions from GXMunt plotted against polar angle for four ducts of different hub tip ratio $\nu = 0, 0.2, 0.5, 0.75$. The red lines on each plot show the difference between the amplitude predicted for the cylindrical duct case and the amplitude predicted for the other ducts. While plotted for all cases, only the difference in the high hub-tip ratio case ($\nu = 0.75$) is clearly visible on the plot as the difference in other cases is small and often negligible. (a) $m = 22$, $\widehat{k_0} = 25$. (b) $m = 11$, $\widehat{k_0} = 14$. (c) $m = 6$, $\widehat{k_0} = 8$. (For interpretation of the references to colour in this figure legend, the reader is referred to the web version of this article.)

Table 5
Reflection coefficients obtained from GXMunt for the $m = 11$, $n = 1$, $\widehat{k_0} = 14$ case highlighting ratio of the reflected to transmitted modal amplitudes.

Hub-tip ratio, ν	$\lvert A^+_{mn}/A^-_{mn}\rvert$
0	0.1171993
0.2	0.1171993
0.5	0.1158121
0.75	0.0847448

For the intermediate azimuthal mode case ($m = 11$), a variation in predicted far-field amplitude is observed only in the annular case with the highest hub-tip ratio ($\nu = 0.75$), where a difference in peak amplitude of around 2.5 dB is shown. These effects are further accentuated for the lowest azimuthal mode considered ($m = 6$), where the difference in peak amplitude becomes around 3 dB (between the highest hub-tip ratio case and the circular case). At the lowest azimuthal mode, there is also a difference, though small (< 0.5 dB), in the hub-tip ratio $\nu = 0.5$ case.

Fig. 14 also highlights the difference far-field amplitude between the baseline and annular duct cases in red. Notably, varying the hub-tip ratio does not result in an amplitude variation consistent across all polar angles. The largest deviations are observed at angles below 90 degrees (that is, upstream of the highlight plane of the intake). Above 90 degrees, there is a negligible difference as the hub-tip ratio of the duct is increased.

For the lowest frequency case (Fig. 14c), the biggest difference observed for the highest hub-tip ratio is at a polar angle of around 55 degrees which coincides with the predicted peak amplitude for that duct. In comparison, for the other ducts, the peak amplitude is at a higher polar angle of around 65 degrees. Hence, as well as causing an increase in predicted amplitude, increasing the hub-tip ratio can also shift the observed peak polar position of this amplitude in extreme cases.

The deviations in far-field amplitude observed between ducts with different hub-tip ratios in this section highlight potential sources of far-field radiation error. One possible explanation for these differences relates to variations at the duct exit plane. Specifically, changes in the ratio of the reflected to transmitted modal amplitudes between ducts of different hub-tip ratios could contribute to the observed trends. To investigate this, the self-reflection coefficients at the duct exit plane were obtained, defined as $\lvert A^+_{mn}/A^-_{mn}\rvert$, where $A^{\pm}_{mn}$ are the amplitudes of the reflected and transmitted pressure modes, respectively. These coefficients allow assessment of whether the increased far-field amplitude in high hub-tip ratio cases arises from a reduction in the amplitude of the wave reflected back into the duct.

For the $m = 11$, $n = 1$, $\widehat{k_0} = 14$ case, the self-reflection coefficients are presented in Table 5. The results show that, as the hub-tip ratio increases, the relative amplitude of the reflected acoustic mode is lower, as indicated by the decreasing coefficient. The effect is most pronounced for the highest hub-tip ratio ($\nu = 0.75$), where a reduction of approximately 25% is observed relative to the circular duct case. This is consistent with the increased far-field amplitude seen in Fig. 14b and is likely the main effect observed.

Another potential factor influencing the observed differences is the effect of the centre body in the region beyond the duct, which may induce additional reflections contributing to the radiated sound field. It should also be recognised that the observed discrepancies inherently include contributions from source truncation errors. However, since a correction is applied to the far-field amplitude to effectively conserve the same in-duct upstream acoustic energy flux, amplitude errors due to source truncation are expected to be minimal. Phase errors may also be introduced according to earlier findings of the study. However, these would not be appreciable in the current analysis as only independent mode radiation is considered.

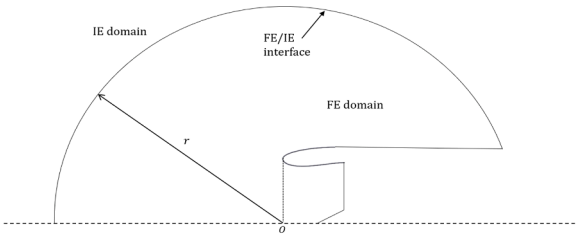

Fig. 15. Circular CAA FE/IE domain with origin O and radius r.

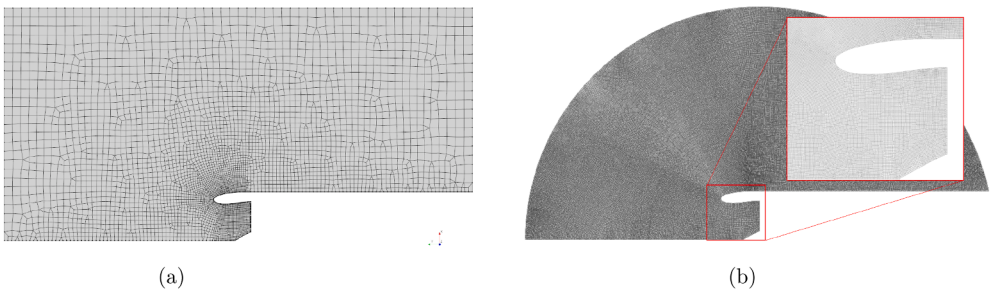

Fig. 16. The computational meshes used for linear CAA analysis. (a) Mesh used to calculate the mean flow in ACTRAN's Euler flow solver. (b) Mesh used to calculate acoustic propagation through the intake and into the far-field.

3. Linear CAA for far-field propagation with a realistic axisymmetric intake

This section demonstrates an application of the part-span approximation with a Computational Aeroacoustics (CAA) method for linear propagation of tone noise through an axisymmetric but otherwise realistic intake geometry and to the far-field. Three cases are considered:

- Cut-on rotor-locked tone noise propagation through 2D axisymmetric mean flow,
- 2D axisymmetric mean flow with high-order radial modes close to the cut-off/cut-on boundary,
- 3D rotor-locked tone noise propagation through distorted mean flow.

For each case, the part-span methodology is applied at two hub-tip ratios (specified at the source plane), where the 'artificial' hub wall is defined by a streamtube according to the mean flow in the domain.

3.1. Method

The commercial software ACTRAN, a frequency domain Finite Element (FE)/Infinite Element (IE) code, is used in the manner of previous similar applications [8,54,55]. The software is based on the convected Helmholtz formulation for the acoustic velocity potential, uses modal boundary conditions for the acoustic source, and employs rigid-wall duct modes for the incident acoustic field. A non-reflective condition is applied at the source plane to account for reflections from duct geometry variations upstream. A 2D view of the axisymmetric domain used for acoustic analysis in the full domain case is shown in Fig. 15. The FE domain is discretised into finite elements, with nodes defined at element vertices and is bounded by an IE layer on the outer boundary which is employed for propagation to the free field in cases. Viscous effects are omitted.

The mean flow was calculated for each full domain case in ACTRAN using the in-built Euler flow solver. The flow was computed using a computational domain with clear upstream and downstream axial boundaries, highlighted in Fig. 16a for the 2D axisymmetric cases. For the 3D case, the upstream, downstream and adjacent boundaries were inclined according to the flight stream angle of attack. In all cases, the flight stream Mach number was around 0.4 and the Mach number at the exit plane in the intake duct was around 0.6. For the 3D distorted case, a flight stream angle of attack of 3.57 degrees was used. The computed flow field was then interpolated onto the mesh used for acoustic analysis (shown for the 2D full domain case in Fig. 16b). In the IE domain, probe points were positioned in an arc at a radius of 40 m from the origin O, representing the far-field propagation sample points. In the 3D case, two far-field arrays of probes were used, as highlighted in Fig. 17. This method has previously been validated for a case with a general intake geometry [56].

Table 6 shows the cases considered in this section. The first cases (A) are designed to be comparable to those in the analytical far-field predictions (Section 2.4) and are representative of instances where rotor-locked, well cut-on modes are considered. The next case (B) considers a high-order azimuthal and radial mode that is close to the cut-off/cut-on boundary and involves mode transition through the duct propagation region. The final case (C) investigates the part-span approximation for a case with 3D distorted intake flow due to a flight stream angle of attack.

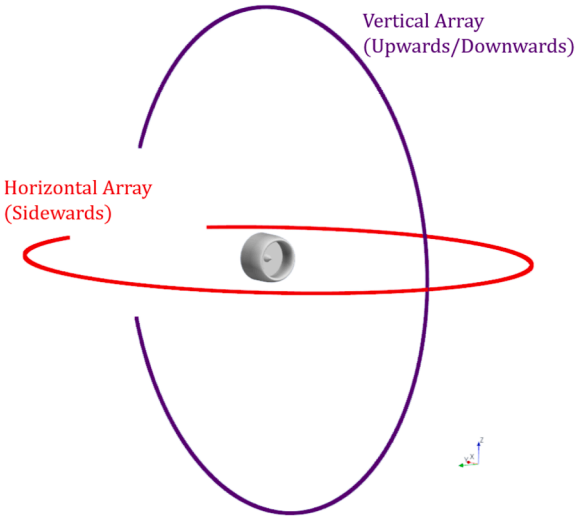

Fig. 17. Probe positions in the infinite element domain for the 3D CAA case.

Table 6
Test matrix showing the cases considered in the following far-field predictions. [1]Mach number at the source plane in the domain.

Case	Domain	Azimuthal Harmonic, m	Radial Harmonic, n	Frequency, $\hat{k}_0$	Mach number[1], M	Hub-tip ratio, ν
A	2D	22	1	22.2	0.61	Full domain, 0.5, 0.75
		11		11.1		
		6		6.9		
B	2D	44	3	44.2		
C	3D	22	1	22.2		

In all cases, the full domain case has an axisymmetric but otherwise realistic nacelle and spinner geometry. The part-span domains have the same nacelle geometry. Two hub-tip ratios are considered at $\nu = 0.5$ and $\nu = 0.75$. The 'artificial' hub walls in the part-span cases are defined using a streamline (or streamtube for the 3D case) derived from the computed mean flow. This is obtained by placing a seed at the specified hub-tip ratio on the source plane and propagating it upstream through the domain. In this way, the domain geometry in the part-span cases is valid for the computed flow field. By contrast, Daroukh et al. [57] employed a uniform hub wall for the non-linear propagation of a shock-associated tonal noise field in an intake and found that the mean flow was not preserved, which contributed to variations in the propagated acoustic field. For this reason, a streamtube definition is preferred in the present study to avoid introducing additional errors due to mean-flow variations.

For the 2D axisymmetric simulations, the acoustic domain extended to a radius of three inner duct radii. The mesh size for the domains employing a part-span approximation with hub-tip ratios of $\nu = 0.5$ and $\nu = 0.75$ corresponded to approximately 65% and 33%, respectively, of the mesh required for the full-domain case. For the 3D simulations, the acoustic domain extended to a radius of 2.5 duct radii. The mesh sizes for the part-span domains were approximately 95% and 90% of that of the full-domain mesh, which contained around 110 million elements. The mesh savings in the 3D cases were almost directly proportional to the differences in domain volume. The smallest cells in all computational meshes were located near the inner lip of the intake, where the local velocity was greatest.

At the source plane, the modal duct boundary condition in ACTRAN was applied, specifying the inner radius, outer radius, harmonic order, and frequency. As highlighted in Section 2.4, the far-field amplitudes were scaled such that the acoustic energy flux of the incident mode was consistent across all hub-tip ratios.

3.2. Results

3.2.1. Case A - Cut-on rotor-locked tone noise propagation through 2D axisymmetric mean flow

The flow computed for the 2D cases in this study is highlighted in Fig. 18. This full-domain flow field was interpolated onto each acoustic domain prior to the FE acoustic simulations.

Fig. 19 shows a contour plot of acoustic pressure for the highest azimuthal mode case ($m = 22$) in the full domain and the part-span domain with a hub-tip ratio of 0.5. The contours show the in-duct and near-field radiation, as well as the initial directivity of the fluctuations, which look sensible for both domains. This observation was made for all instances, though plots are not shown for brevity.

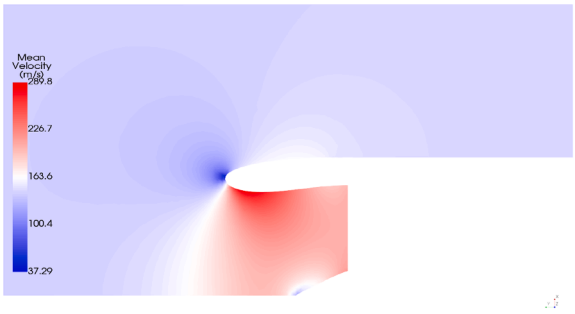

Fig. 18. The full domain mean flow field computed in ACTRAN's Euler flow solver and interpolated onto the domain used for acoustic analysis.

Fig. 19. Pressure field in the FE domain for the rotor-locked $m = 22$ mode calculated in ACTRAN for both full and part-span ($\nu = 0.5$) domains. (a) Full domain. (b) Part-span domain ($\nu = 0.5$).

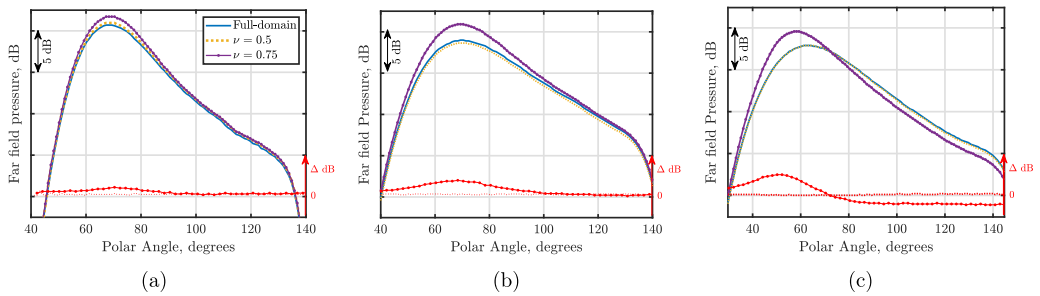

Fig. 20. Far field amplitude plotted as a function of polar angle for three azimuthal modes (at three different frequencies) for a full domain and two part-span domains. For each mode, only a single radial mode is cut-on. The red lines on each plot show the difference between the amplitude predicted for the cylindrical duct case and the amplitude predicted for the other ducts. While plotted for all cases, only the difference in the high hub-tip ratio case ($\nu = 0.75$) is clearly visible on the plot as the difference in other cases is small and often negligible. (a) $m = 22$, $\widehat{k_0} = 22$. (b) $m = 11$, $\widehat{k_0} = 11$. (c) $m = 6$, $\widehat{k_0} = 7$. (For interpretation of the references to colour in this figure legend, the reader is referred to the web version of this article.)

This test case aims to extend the understanding of the impact of a part-span approximation on far-field directivity by introducing flow and geometrical effects. Fig. 20 presents the far-field amplitude against polar angle for each case.

At the highest azimuthal mode ($m = 22$), the predicted far-field amplitude deviates a maximum of 1 dB between all cases. For the intermediate domain (with $\nu = 0.5$), a deviation of less than 0.3 dB is observed across all polar angles. For the highest hub-tip ratio domain ($\nu = 0.75$), there is a maximum difference of 1 dB at a polar angle of around 70 degrees, which coincides with the polar angle where the overall peak amplitude is observed. Away from the peak, the difference is much smaller and mostly negligible. The analytical predictions at a comparable frequency and harmonic showed similar differences suggesting that the introduction of a mean flow and non-uniform geometry is not significant to the error in the far-field amplitude at this mode/frequency.

At the intermediate azimuthal mode considered ($m = 11$), the part-span domain with hub-tip ratio $\nu = 0.5$ shows a mostly consistent deviation from the baseline case of less than 0.5 dB across all polar angles. At the higher hub-tip ratio of $\nu = 0.75$, there is a more significant deviation of up to 2.5 dB, which is a maximum at a polar angle of around 70 degrees, also coinciding with the angle at which the peak level is observed. This deviation is similarly consistent with the far-field predictions of the previous section.

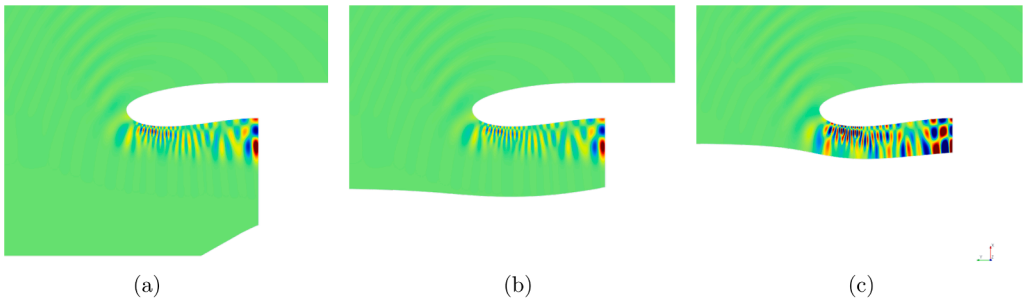

Fig. 21. Contours of the real part of acoustic pressure in each domain for a mode which is close to the cut-off/cut-on boundary with an azimuthal harmonic of $m = 44$, a radial harmonic of $n = 3$, and a frequency of $\widehat{k_0} = 44.2$. (a) Full domain. (b) $\nu = 0.5$. (c) $\nu = 0.75$.

For the lowest azimuthal mode investigated ($m = 6$), once again, a negligible difference is observed between the baseline case and part-span domain with a hub-tip ratio of $\nu = 0.5$. For the highest hub-tip ratio case ($\nu = 0.75$) a maximum difference of 4 dB is observed at a polar angle around 55 degrees. As was observed in the previous section, this high hub-tip ratio (and low azimuthal mode) also causes the polar angle of the peak amplitude to be shifted lower by around 10 degrees. Compared with the analytical work previously presented, the findings are consistent, highlighting negligible difference in far-field amplitude between the full domain and hub-tip ratio of $\nu = 0.5$ cases, and more notable differences in the far-field between the full domain and high ($\nu = 0.75$) hub-tip ratio case.

For the three modes shown here, the impact of a moderate ($\nu = 0.5$) part-span approximation on far-field amplitude (far-field radiation errors) is low in most cases. When an 'extreme' hub-tip ratio ($\nu = 0.75$ in this case) is applied, far-field radiation errors are observed, particularly for low azimuthal harmonics. The deviations are not consistent across all polar angles and are more significant for polar angles below 90 degrees. This effect was similarly identified in the previous analytical far-field section (Section 2.4) and dummyTXdummy-(was suspected to be the result of a change in the reflection coefficient at the duct plane exit. While that reflection coefficient data is not presented for the current CAA cases, it is a potential reason for the observed deviations.

3.2.2. Case B - 2D axisymmetric mean flow with a high-order radial mode close to the cut-off/cut-on boundary

This test case is designed to challenge the capabilities of the part-span approximation by considering the propagation and radiation of a relatively high-order radial mode close to the cut-off/cut-on boundary. The incident mode has an azimuthal harmonic of $m = 44$, radial harmonic of $n = 3$ and frequency of $\widehat{k_0} = 44.2$. In this case, mode transition is also observed, that is where the state (cut-off/cut-on) of the mode varies during propagation through the intake duct. Mode transition cases are of interest and have been previously reported [58].

This case was selected as it may be representative of an applied scenario, such as the rotor-locked 2BPF mode. In light of the findings presented earlier, it also constitutes a feasible candidate for the part-span approximation, since a substantial portion of the modal energy remains concentrated near the outer wall of the intake due to the high azimuthal order of the mode. However, given its proximity to the cut-off/cut-on boundary, earlier analysis (Section 2.2) suggests that such a case may be more susceptible to large in-duct errors. The impact on the far-field amplitude was expected to be limited, since modes close to the cut-on/cut-off boundary, although often with high in-duct modal amplitude, can exhibit reduced contribution to the far-field radiation owing to low radiation efficiency and possible partial cut-off over the duct length.

The incident mode is initially cut-on at the source plane and quickly transitions to a cut-off state, resulting in an initial decay of amplitude through the intake. Due to flow acceleration around the intake lip (highlighted in Fig. 16a), the mode becomes momentarily cut-on before transitioning back to cut-off further upstream, where the velocity decreases ahead of the intake highlight. Although the mode remains cut-off at the upstream end of the intake duct, it retains an appreciable amplitude and contributes to far-field radiation. Consequently, both the in-duct acoustic pressure field and the far-field amplitude are considered in the analysis.

Fig. 21 presents in-duct contours of the real part of the acoustic pressure within the intake for each domain. As the mode propagates through the duct, amplitude variations can be observed due to the transitions between cut-on and cut-off conditions. Upstream of the intake, variations in the contours also indicate that some of the acoustic energy is radiated to the far-field.

Visually, there is little difference between the full-domain case and the case employing the part-span approximation with a hub-tip ratio of $\nu = 0.5$. In contrast, for the higher hub-tip ratio case ($\nu = 0.75$), a more pronounced variation in the in-duct acoustic pressure field is observed. As illustrated in Fig. 21c, the part-span domain in this case intersects the modal content at the source plane, which likely contributes to the differences observed along the duct. The axial location at which the mode initially transitions from cut-off to cut-on shifts in the high hub-tip ratio case, as the solution of the radial eigenvalue, and therefore the axial wavenumber, varies with this combination of mode order and hub-tip ratio relative to the full-domain case. Consequently, the transition point moves further upstream within the intake duct, which can be identified by the extended axial region of high amplitude from the source plane.

The far-field amplitudes across a range of polar angles are shown in Fig. 22 for each domain. Consistent with the earlier far-field data, the present results have been scaled according to the acoustic energy flux of the upstream-travelling incident wave in each case.

A similar polar directivity pattern is observed to that of the $m = 22$, $n = 1$ case (Fig. 20a). The peak amplitude occurs at a polar angle of approximately 70 degrees and is accurately predicted in all domains, with only small variations in level between cases. For

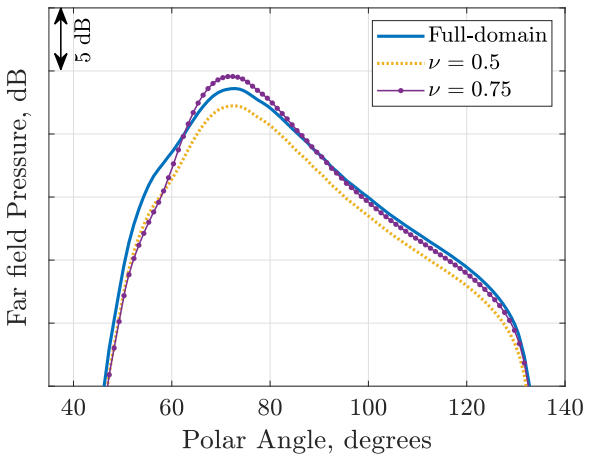

Fig. 22. Far-field amplitude plotted as a function of polar angle for a mode close to the cut-off/cut-on boundary in the intake duct with an azimuthal harmonic of $m = 44$, a radial harmonic of $n = 3$, and a frequency of $\hat{k_0} = 44.2$.

the case employing the part-span approximation with a hub-tip ratio of $\nu = 0.5$, the shape of the polar directivity is well captured, while the amplitude differs by around 1.5 dB from the full-domain prediction across most polar angles. For the highest hub-tip ratio case ($\nu = 0.75$), the predicted amplitude is slightly higher than the baseline at the peak polar angle. At higher polar angles ($> 70°$), this case agrees within 0.5 dB of the baseline, whereas at lower angles the amplitude is under-predicted relative to the baseline.

Overall, the variations observed between each domain suggest that, for modes close to the cut-off/cut-on boundary, the part-span approximation can still predict the far-field amplitude with reasonable accuracy. Small deviations are evident, although their significance is application dependent. In multimode cases that include other well cut-on modes, those close to the cut-off/cut-on boundary are expected to have a limited influence in the far field, as their contribution will be much lower in amplitude relative to the dominant cut-on modes. For the present study, for example, the more strongly cut-on first- and second-order radial modes at the same frequency and azimuthal order exhibited peak far-field amplitudes approximately 20 dB and 10 dB higher, respectively, than the mode considered here, assuming the same incident intensity for each mode at the source plane.

3.2.3. Case C - 3D rotor-locked tone noise propagation through distorted mean flow

The final case employs a larger 3D FE domain to simulate a distorted mean flow field. The aim of this case is to address the methodology's applicability when 3D effects are considered. To impose the distorted field, a shallow flight stream angle of attack of 3.57 degrees is used. As a result there is a circumferential inhomogeneity in the intake due to the greater acceleration of flow around the bottom lip of the nacelle. Fig. 23 highlights the variation in axial velocity through the intake duct as flow is more significantly accelerated at around the bottom lip of the intake relative to the top.

Contours of the real part of the total acoustic pressure field at different axial locations are shown in Fig. 24. Throughout this section, the total acoustic field is considered. As a result, while only an upstream travelling incident mode at fixed azimuthal and radial order, the resultant total acoustic field includes both upstream and downstream components of all contributing azimuthal and radial modes.

At the source plane, the incident $m = 22$, $n = 1$ mode is dominant, although some other azimuthal variation is evident due to the local flow non-uniformity at that location. At the throat, a more complex distribution of acoustic pressure is observed in all cases, with much of the acoustic energy flux directed toward the outer wall of the duct. Further upstream, the onset of radiation toward the far field becomes visible. The spiralling structure characteristic of a spinning mode is apparent; however, an azimuthally uniform pattern is not observed due to the distortion introduced by the inclined ambient flow. This causes parts of the mode to radiate in the direction of the flow while others radiate against the inclined flow component. Across the different domains, small variations are present, though the dominant trends remain consistent between cases.

The axial evolution of the same quantity is also highlighted in Fig. 25. This view also highlights the domain variation due to the implementation of a part-span approximation with streamtube's defining the artificial inner wall. Generally, the variation of the acoustic field through the intake duct appears consistent between each domain. Key features include the 'bunching' of acoustic content toward the bottom lip due to the increased flow velocity against the propagating acoustic field. Additionally, upstream of the intake, the radiating acoustic field appears to be more significant in the upwards direction, also a result of the local distorted flow around the intake lip. These effects appear to be predicted well in both part-span approximation applications. Some small variations are visibly observed toward the top of the intake duct in the high hub-tip ratio application.

To further investigate the in-duct acoustic field for each domain, Fig. 26 shows azimuthal mode distributions at two axial locations in the intake: the source plane and the throat position. This distribution is generated by completing a spatial Fourier transform in the azimuthal direction of the total acoustic pressure field on the nacelle wall. As a result, it is noted that both upstream and downstream components are included in the mode distributions and radial components are not separated out.

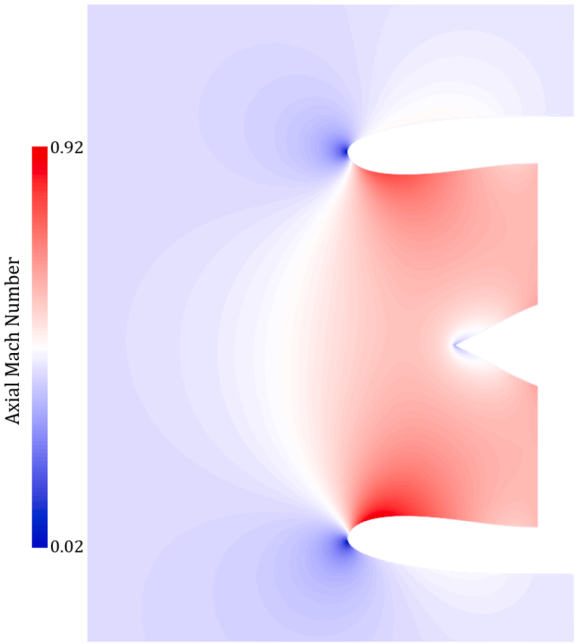

Fig. 23. Side-on planar view of the variation of axial Mach number in the FE domain for the 3D distorted flow case case.

At the source position (Fig. 26a), the $m = 22$ azimuthal component dominates the distribution, exhibiting an amplitude approximately 10 dB higher than any other component. The amplitude of this mode is slightly under-predicted in both part-span cases, by up to 4 dB. The spectra exhibit a global level shift in each domain, indicating that while the absolute amplitudes differ, the relative distribution of dominant components is preserved.

Following propagation through the intake to the throat position, the azimuthal distribution changes significantly due to the influence of the azimuthally non-uniform mean flow on the modal acoustic field. Physically, this interaction results in a scattering of modal content across different azimuthal orders - an effect that has been investigated in previous studies, for example [7].

At the throat position (Fig. 26b), the dominant azimuthal components in all cases correspond to the immediately neighbouring components ($m = 21$ and $m = 23$) of the original rotor-locked component ($m = 22$). The scattering effect continues to distribute acoustic energy across a wider range of azimuthal harmonics, with more energy transferred toward higher azimuthal orders in this case. This behaviour is attributed to the high flow velocity at this axial location, which shifts the cut-off/cut-on boundary to higher azimuthal orders. In the present case, the estimated cut-off/cut-on boundary-assuming a uniform annular duct and using the azimuthally averaged mean flow at 95% span-occurs at $m = 32$. Consequently, the higher-order modes near this boundary are expected to contribute less to the overall far-field sound.

Nevertheless, compared with the full-domain case, the part-span approximation cases capture the mode-scattering behaviour reasonably, showing only small amplitude discrepancies. Across the dominant azimuthal components, the differences are approximately 1 dB and 4 dB for the $\nu = 0.5$ and $\nu = 0.75$ cases, respectively, which is similar to those observed for the rotor-locked $m = 22$ component at the source plane. These results therefore indicate that a high hub-tip ratio part-span approximation can be applied to in-duct propagation problems where three-dimensional effects are significant, with reasonable accuracy.

The amplitude of the total acoustic pressure field in the far field is now examined in Fig. 27. Four far-field positions are shown, corresponding to the array locations highlighted in Fig. 17.

Fig. 27a presents the amplitude as a function of polar angle directly above the intake. The overall envelope of the response is broadly similar to that observed for the single $m = 22$ mode case in Fig. 20a. However, the response here is more complex, exhibiting greater variation in amplitude across a wider polar range. The peak laevel occurs just below 40 degrees. Below the intake, the peak level is approximately 25 dB lower, as highlighted in Fig. 27b. This behaviour is attributed to the inclined mean flow effect causing local flow variations between the top and bottom lip of the nacelle, resulting in an apparent redirection of acoustic energy towards the upper hemisphere, a trend also reported in previous studies [15].

The far-field amplitudes at the lateral positions are shown in Fig. 27c and d. Although the peak levels on both sides differ by less than 1 dB, the envelopes show a clear asymmetry. This arises from the spinning nature of the radiated acoustic mode: on the port (right) side of the intake, higher amplitudes are sustained across a wider polar range, whereas on the starboard (left) side the radiation pattern is more directional.

A broad comparison between the full-domain case and the part-span approximations shows that the $\nu = 0.5$ case provides a good prediction of the far-field amplitude at all observer locations. Larger deviations occur only in regions where the sound level is already low (e.g., below 40 degrees in Fig. 27b & c), and therefore of limited practical significance. For the higher hub-tip ratio case

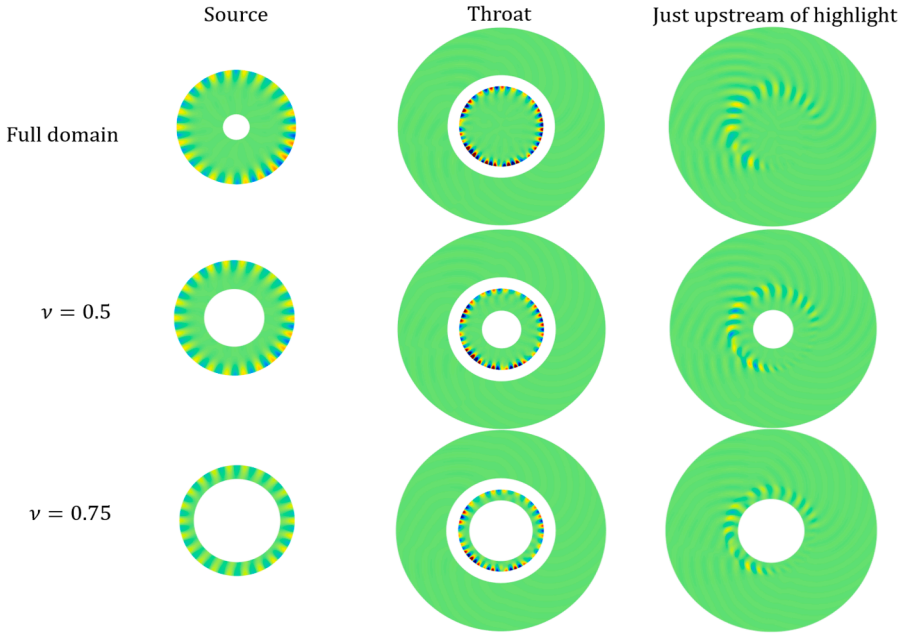

Fig. 24. Planar views of the real part of acoustic pressure at different axial positions.

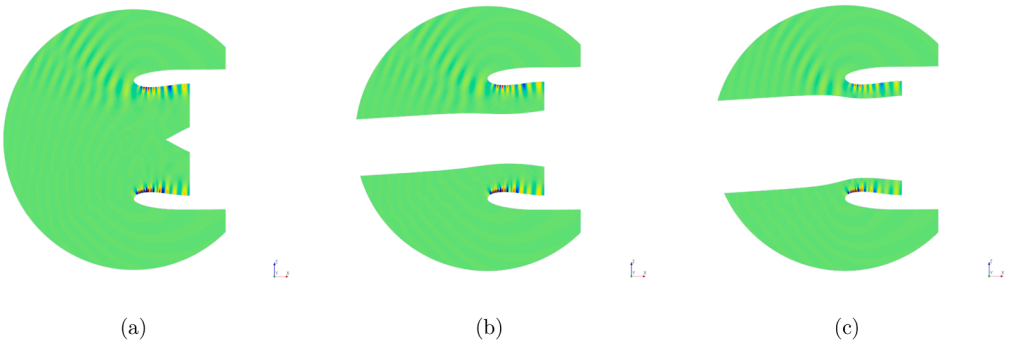

Fig. 25. Real part of acoustic pressure in the FE domain for each test case. (a) Full domain. (b) Part-span approximation with $\nu = 0.5$. (c) Part-span approximation with $\nu = 0.75$.

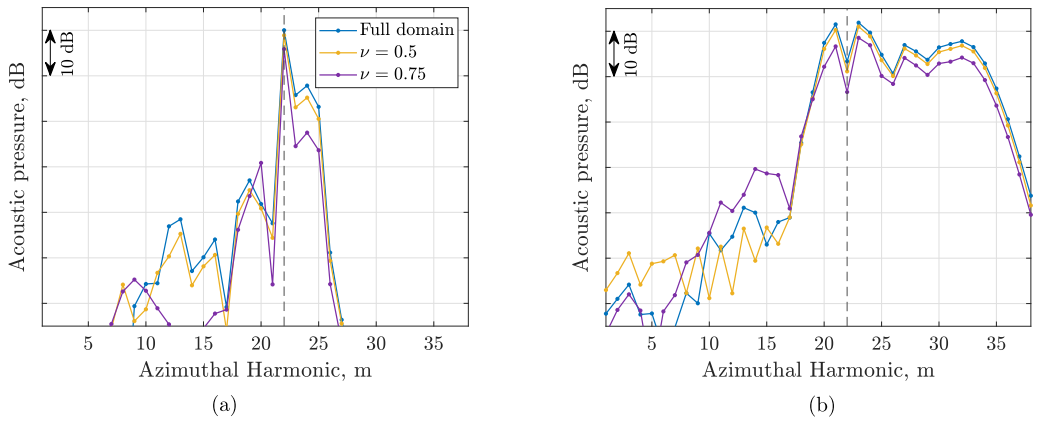

Fig. 26. Azimuthal mode distributions of the total acoustic field on the nacelle wall at two axial positions in the intake duct. (a) Source plane axial position. (b) Intake throat axial position.

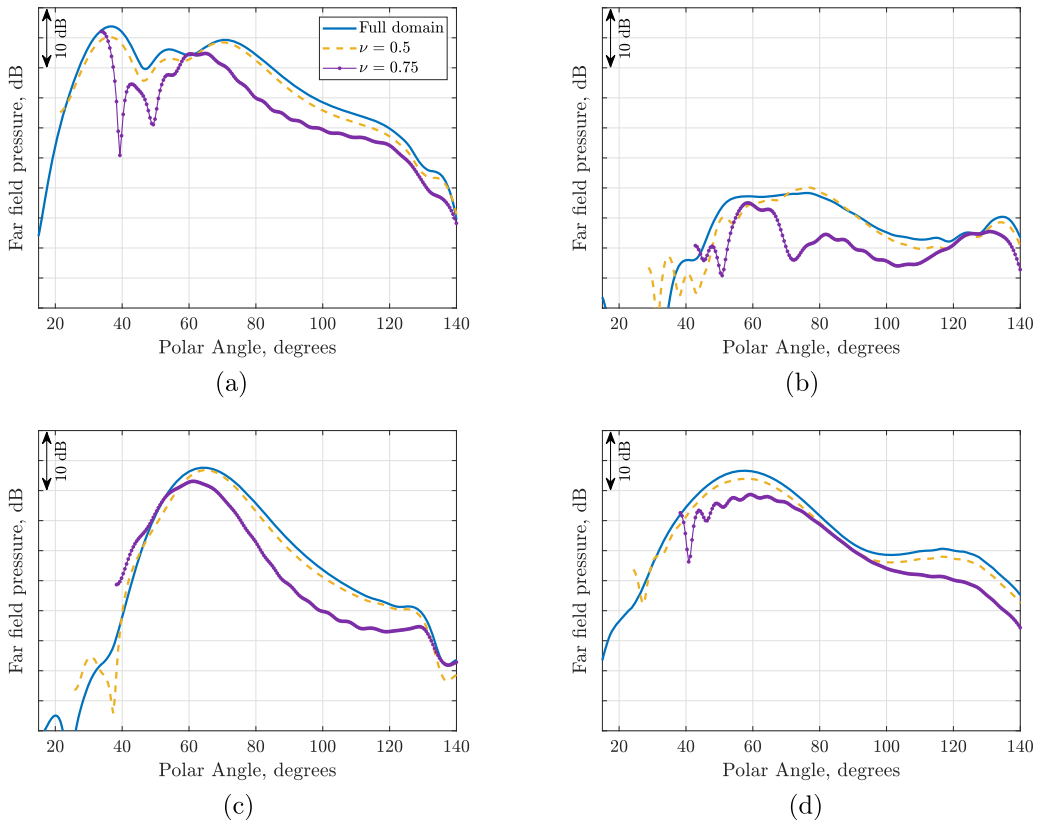

Fig. 27. Far-field predictions of the total acoustic field for each domain and for four far-field locations. The probe positions are highlighted in Fig. 17. (a) Vertical array, upwards. (b) Vertical array, downwards. (c) Horizontal array, left-side (looking into intake). (d) Horizontal array, right-side.

($\nu = 0.75$), more noticeable discrepancies are observed. Furthermore, the introduction of the artificial hub wall restricts the range of polar positions for which the far-field can be predicted.

These findings suggest that the influence of the part-span approximation can become significant in cases involving three-dimensional effects and when a high hub-tip ratio is applied. However, they also indicate that, for many practical configurations, a moderate hub-tip ratio can be employed while still achieving a far-field amplitude prediction with good fidelity.

4. Summary

This paper has investigated acoustic mode propagation in ducts of varying hub-tip ratios to appreciate the impact of introducing a *part-span approximation* for analysis of aeroengine intake tone propagation and radiation. The first sections presented analytical studies in uniform ducts with uniform mean flow, considering isolated mode shape representations, the effects on axial wavenumber, and axial propagation characteristics. Subsequently, the influence on far-field radiation was evaluated using an analytical model for a uniform duct. Finally, a computational aeroacoustics (CAA) approach was employed to investigate the application of a part-span approximation with an axisymmetric, yet otherwise realistic, intake geometry. Three cases were considered, ranging from single cut-on acoustic modes (likened to rotor-locked modes) in a two-dimensional axisymmetric mean flow, through to a distorted configuration addressing three-dimensional effects.

The study has identified a number of potential errors introduced by a part-span approximation which can be categorised into three groups: **source truncation error**, **in-duct propagation error**, and **far-field radiation error**.

Source truncation errors are related to the representation of the initial profile in terms of acoustic modes in the part-span domain. Many of these errors relate to cut-off modes which die away in the initial propagation region. Beyond this region, the error remains constant and does not grow with further propagation.

1. When the position of the artificially introduced hub boundary truncates a pressure profile any acoustic energy at lower radii is neglected.
2. Truncating the input profile introduces high-order radial modes in the part-span duct. If these high-order modes are cut-off, they die away during initial propagation, giving rise to an error in the pressure profile shape and amplitude. An equivalent result would be achieved by using only the cut-on part-span modes to represent the original profile.

3. The higher part-span inner wall radius is capable of artificially making one or more radial modes in the part-span duct become cut-on which are otherwise cut-off in the full-span duct. This can give rise to large errors in the in-duct pressure amplitude and is a potential limitation of the methodology, although it is noted that these just cut-on modes will carry relatively little acoustic power, and hence the error in the predicted far-field noise is likely much smaller. A similar effect may be observed if modes are 'nearly cut-on' in the part-span duct, such that the decay rate is sufficiently low that they can still (together with a reflected cut-off wave) propagate acoustic energy to the intake highlight plane.

In-duct propagation errors are related to the axial wavenumbers in the part-span duct and tend to grow over the propagation distance.

4. Even for only a single cut-on mode in the part-span duct, a higher artificial inner wall changes the axial wavenumber k_z, giving rise to a phase error in the propagated profile. Such phase errors can be important, though if the calculation objective is far-field noise amplitude, this error can be safely neglected.
5. If multiple cut-on modes are present in the part-span duct, they interfere constructively and destructively, both in-duct and in the far-field. This interference is phase dependent, and the errors in axial wavenumber, giving rise to phase errors in each of the cut-on modes, will affect the pressure amplitude. For the axisymmetric case with uniform mean flow, the total sound power level will be unaffected by this interference effect. In the general case, the error in sound power level is still expected to be small. In terms of far-field directivity, however, the part-span approximation will be less accurate at single frequencies and circumferential harmonics with more than one cut-on radial mode.

   In an axisymmetric rotor-locked field, circumferential harmonics are directly related to frequency. In the presence of inflow distortion, however, various circumferential modes can be present at the same frequency and this type of error from interfering modes will also be present in the predicted far-field azimuthal directivity.
6. For cut-off modes that are close to cut-on (together with a reflected cut-off wave), acoustic energy can be carried to the far-field [59] giving rise to phase and amplitude errors in-duct and in the far-field. For mode transition cases, where the mode state changes during propagation through the duct, the transition positions can vary when an artificial hub wall, causing amplitude differences through the duct.

The third group of potential errors are related to **far-field radiation**.

7. For isolated acoustic modes radiating from annular ducts with an infinite centre body with 2D axisymmetric flow, an over-prediction of far-field amplitude is sometimes observed. This effect is more significant at lower polar angles, for lower azimuthal modes, and high hub-tip ratio ducts. Comparisons between analytical predictions assuming a uniform duct with no flow and a linear CAA calculation with axisymmetric intake and mean flow showed almost identical effects due to the increase of duct hub-tip ratio. This over-prediction is likely linked to the radiation impedance at the exit plane of the duct and the presence of the hard-walled centre body surface extending upstream.
8. For high-order radial modes close to the cut-off/cut-on boundary, small deviations in far-field amplitude are related to the sensitivity of the mode transition axial locations which can change when the part-span approximation is applied.
9. When 3D flow is considered, multiple modal components are introduced due to the interaction of the acoustic field and mean flow field. The amplitude of the total acoustic field can be well predicted across a range of azimuthal and polar ranges for a moderate hub-tip ratio part-span approximation. When high hub-tip ratios are applied, greater differences are observed.

Source truncation errors were introduced in Section 2.1 and better understood in Section 2.3 following Bessel decomposition of truncated modes at the source plane, highlighting how multiple high-order radial modes are required to represent such modes in ducts with higher hub-tip ratios than the baseline. Highlighting the error over propagation (as in Fig. 13) shows an increase in error over a short initial propagation period before stabilising for high circumferential modes. In contrast, at lower circumferential harmonics, in-duct propagation error is highlighted as the error deviates over the propagation region due to interference between cut-on radial components.

Generally, implementation of a part-span approximation introduced the least overall error for high circumferential mode orders which often have little signal content at low radii. Where a significant region of signal content was truncated, more error was identified. Ensuring less than 1% of acoustic energy was truncated achieved an error of less than 2% in the mode shape representation and value of axial wavenumber.

Far-field analysis showed reasonable predictions in all cases when a part-span approximation with hub-tip ratio of 0.5. At the highest hub-tip ratio considered ($\nu = 0.75$), deviations were observed in far-field amplitude in all cases, but the extent varied depending on the modal content considered. Three dimensional effects on the acoustic radiated field were well predicted with a moderate hub-tip ratio application.

The findings of this study regarding mode shape representation and propagation in ducts with varying hub-tip ratios can inform the development of a full-span application with optimised radial mesh density and discretisation of the full physical domain. Optimising the number and spacing of cells would enable accurate resolution of the acoustic field across all azimuthal and radial harmonics of interest. Coupled with azimuthal direction optimisation (informed by additional analysis), this approach could significantly reduce mesh size, resulting in an efficient and optimised in-duct hybrid mesh topology.

5. Conclusions and future work

The linear analysis in this study has demonstrated that the part-span approximation can be successfully applied to aeroengine intake tone noise calculations.

The analytical work shows that the approach is most accurate for high circumferential mode numbers with little signal content at low radii.

The 2D computational meshes applying the part-span approximation were around 35% and 65% smaller for a hub-tip ratio of 0.5 and 0.75, when compared to the full domain case. For the 3D cases, the meshes were around 5% and 10% smaller for the same applications.

Seven potential sources of error have been identified in three groups:

- Source truncation errors relating to the representation of the initial profile in terms of acoustic modes in the part-span domain. The hub-tip ratio should be chosen to ensure that nearly all of the signal power is captured in the part-span region. Modes near the cut-off/cut-on boundary also may not be well represented.
- In-duct propagation errors are related to the axial wavenumbers in the part-span duct and tend to grow over the propagation distance. For cases with a single cut-on mode, this affects the phase but the far-field directivity is unaffected. For cases with more than one cut-on mode, the directivity will be affected but the error in overall sound power is likely to be small.
- Far-field radiation error which may be related to the impedance characteristics at the duct outlet plane and the presence of the centre body in the domain.

An error metric is proposed for comparing in-duct pressure profiles accounting for bulk phase differences which have no effect on far-field noise amplitude.

Far-field predictions were considered applying both an analytic model and a computational approach. An error was observed for high hub-tip ratio cases, particularly at lower azimuthal modes. Primarily, an increase in far-field amplitude was predicted, but this increase was not consistent across all polar angles and was more significant at polar angles lower than 90 degrees. When 3D effects are considered, the deviations for high hub-tip ratio applications are more complex due to the increased number of acoustic modes introduced.

Areas of future work identified during this study include:

- Only linear propagation of tonal noise was considered in the present study. In reality, the in-duct acoustic pressure of rotor-alone tone noise has high amplitude and propagates non-linearly through the duct. An extension of the present work to consider a part-span approximation for non-linear propagation is required.
- The work presented here relates to a hard-walled duct. Further work is required to assess the part-span methodology in acoustically lined ducts.
- As was suggested at the end of Section 4, the findings of this study could be useful for a full-span application, in which the full domain is computationally discretized, but the radial distribution of cells is optimised to suitably resolve the acoustic field without wasting computational resource at low-span regions.

CRediT authorship contribution statement

Joseph S.P. Binns: Writing – review & editing, Writing – original draft, Methodology, Investigation, Formal analysis, Conceptualization; **Long Wu:** Writing – review & editing, Supervision, Investigation, Conceptualization; **Alexander G. Wilson:** Writing – review & editing, Supervision, Investigation, Conceptualization.

Data availability

Data will be made available on request, where possible.

Declaration of competing interest

The authors declare that they have no known competing financial interests or personal relationships that could have appeared to influence the work reported in this paper.

Acknowledgements

The first author is financially supported by the University of Southampton and Rolls-Royce plc. The authors wish to acknowledge Howoong Namgoong and the wider Installation Aerodynamics and Noise Team at Rolls-Royce for their continued support and technical discussions. Brian Tester is acknowledged for providing the GXMunt data presented in section 2.4 and offering guidance and discussion. Rie Sugimoto is acknowledged for her guidance with the ACTRAN calculations completed in the study. The authors acknowledge the use of the IRIDIS High Performance Computing Facility, and associated support services at the University of Southampton, in the completion of this work.

Appendix A. Definition of mode shape error with correction factor used in Section 2.3.

The conventional area-weighted mean square error metric is

$$E = \frac{\int |p - \hat{p}|^2 r \, dr}{\int r \, dr}, \tag{A.1}$$

where p is the part-span domain pressure profile and $\hat{p}$ is the full domain pressure profile. As described in the main text, this definition can lead to large error values due to phase differences between the part-span and full-domain pressure profiles (due to different k_z values). Phase errors that are constant across the span won't, however, affect the far-field noise amplitude. For this reason, the part-span pressure profile was treated to remove this bulk phase error effect by choosing a radially uniform phase correction to minimise the error such that,

$$E = \min_{\theta} \left(\frac{\int |pe^{i\theta} - \hat{p}|^2 r \, dr}{\int r \, dr} \right). \tag{A.2}$$

The error will be minimised when the numerator is minimised - that is, when

$$\frac{\partial}{\partial \theta} \int |pe^{i\theta} - \hat{p}|^2 r \, dr = \int \frac{\partial}{\partial \theta} [(pe^{i\theta} - \hat{p})(p^* e^{-i\theta} - \hat{p}^*)] r \, dr = 0 \tag{A.3}$$

$$\int \frac{\partial}{\partial \theta} [pp^* - p\hat{p}^* e^{i\theta} - \hat{p}p^* e^{-i\theta} + \hat{p}\hat{p}^*] r \, dr = 0 \tag{A.4}$$

Performing the differentiation gives

$$\int [-ip\hat{p}^* e^{i\theta} + i\hat{p}p^* e^{-i\theta}] r \, dr = 0 \tag{A.5}$$

Since these two terms are complex conjugates, this can be instead written as,

$$\int 2\Re[-ip\hat{p}^* e^{i\theta}] r \, dr = 0, \tag{A.6}$$

or, equivalently,

$$\int \Im[-p\hat{p}^* e^{i\theta}] r \, dr = 0, \tag{A.7}$$

or,

$$\Im \left[e^{i\theta} \int p\hat{p}^* r \, dr \right] = 0, \tag{A.8}$$

For this to be true, the argument of $e^{i\theta}$ has to cancel the argument of $\int p\hat{p}^* r \, dr$. That is,

$$\theta = -\Im \left[\ln \left(\int p\hat{p}^* r \, dr \right) \right] + n\pi. \tag{A.9}$$

In this case, the $n\pi$ addition is not necessary and the minimum is achieved at

$$\theta = -\Im \left[\ln \left(\int p\hat{p}^* r \, dr \right) \right]. \tag{A.10}$$

A.1. Worked example

An example is considered to further understand the benefit of using a modified error.

From Fig. 13, the $m = 6$, $f = 400$ Hz case is considered. At the source plane, the amplitude and phase of the mode in both the full and part-span domains are shown in Fig. A.1. At this position, the mode is entirely real and the amplitude profiles are mostly the same. Then, after propagating 2 radii upstream, the amplitude and phase of both modes are shown in Fig. A.2

The difference in profiles after propagating is relatively small in the real part and there is a notable variation in phase across the part-span radius. Fig. A.3 shows the difference in phase between the full and part domain mode shapes in the part-span region. The phase is shown before and after a bulk phase across the radius is added which was calculated according to Eq. A.10.

The standard and modified mean square error between mode shapes is plotted in Fig. A.4. For this case, a small difference is shown between the two errors that increases over the propagation distance and the error is dominated by the artificial introduction of high-order radial modes due to the approximation, as highlighted in Section 2.3.

In comparison, following the same analysis for a different case, the $m = 22$, $f = 800$ Hz mode, the errors are plotted in Fig. A.5, where even in the part-span domain, only a single radial mode is cut-on. Hence, the conventional error is considerably higher over propagation when compared to the modified error. This is due to a variation in the real part of the axial wavenumber causing a bulk phase shift when the part-span approximation is applied. The difference highlights the growing increase in error in the standard mean square-based error due to a bulk phase difference which may be misleading, especially over long propagation regions. The modified error, accounting for this bulk phase variation, has a constant value for most of the propagation distance.

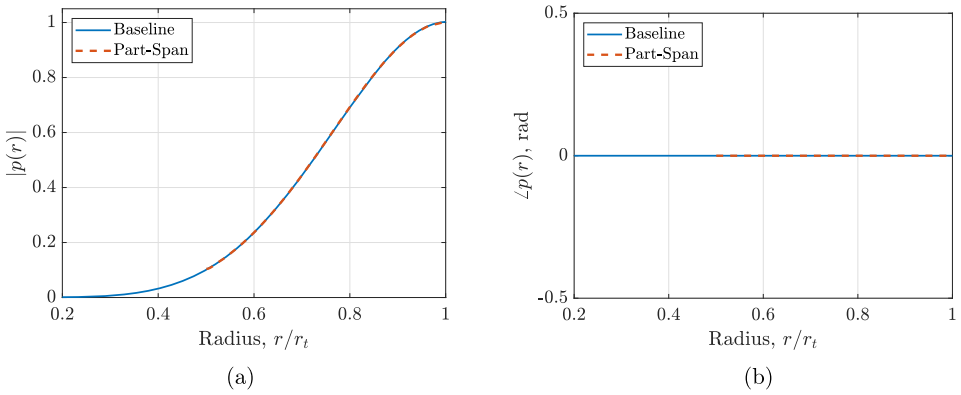

Fig. A.1. Amplitude and phase of full and part domain mode shapes at the source plane. (a) Amplitude of the full and part domain mode shapes at the source plane. (b) Phase of the full and part domain mode shapes at the source plane.

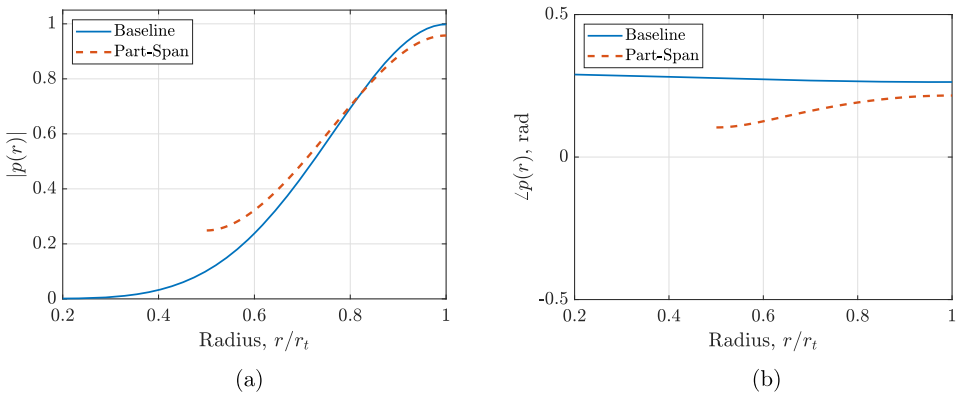

Fig. A.2. Amplitude and phase of full and part domain mode shapes after propagating upstream. (a) Amplitude of the full and part domain mode shapes after propagating upstream. (b) Phase of the full and part domain mode shapes after propagating upstream.

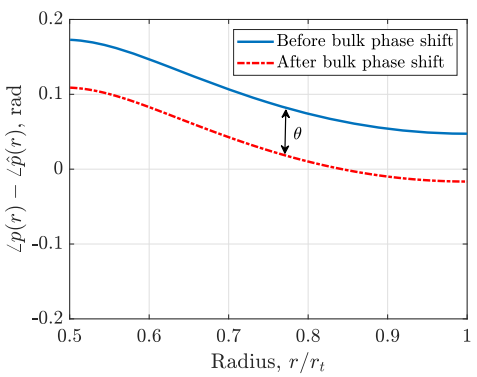

Fig. A.3. The difference in phase between the full and part domain modes in the part-span region.

Finally, the error computed over the propagation region is presented in Table A.1 for the cases introduced in Fig. 13 to highlight the difference between the error definitions. In all cases, the conventional error is greater than the modified one. The difference is most for the highest frequency case where only a single radial mode is cut on in both domains and the phase difference, which is constant over the span, will have minimal impact on far-field predictions. Comparatively, in the other cases, the error is dominated by the introduction of high-order radial modes in the part-span domain, causing local phase variations across the span which may be significant for far-field radiation and directivity predictions.

Table A.1
The error computed over the propagation region of 2 radii for the three cases presented in Fig. 13 according to a conventional mean square-based error and a modified one which accounts for bulk phase differences.

Case	Conventional Error	Modified Error
$m = 22,\ f = 800$ Hz	2.1e-2	1.0e-5
$m = 11,\ f = 600$ Hz	2.3e-3	1.5e-3
$m = 6,\ f = 400$ Hz	0.24	0.18

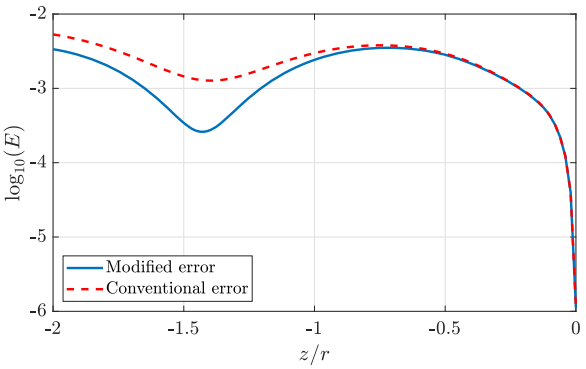

Fig. A.4. The error between mode shapes for the $m = 6,\ f = 400$ Hz case in full and part domains as propagated upstream in a uniform duct. The modified error that accounts for bulk phase differences and a conventional mean square difference are shown.

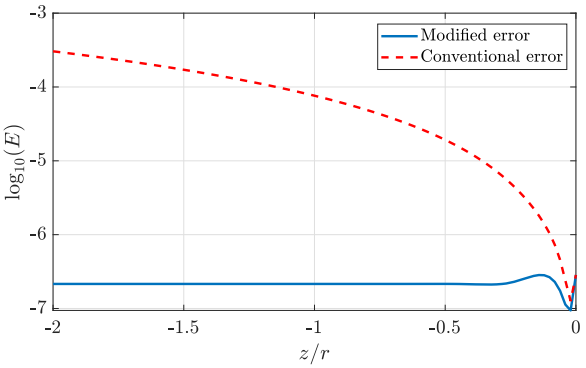

Fig. A.5. The error between mode shapes for the $m = 22,\ f = 800$ Hz case in full and part domains as propagated upstream in a uniform duct. The modified error that accounts for bulk phase differences and a conventional mean square difference are shown.

References

[1] UK-Civil-Aviation-Authority, Aviation noise and health; the effects of aviation noise, 2023, Accessed on 12/05/2023, https://www.caa.co.uk/consumers/environment/noise/aviation-noise-and-health/.
[2] R.J. Astley, Propulsion system noise: turbomachinery, Encyclopedia of Aerospace Engineering (2010) 1–12. https://doi.org/10.1002/9780470686652.eae336.
[3] E. Nesbitt, Current engine noise and reduction technology, CEAS Aeronaut. J. 10 (1) (2019) 93–100. https://doi.org/10.1007/s13272-019-00381-6.
[4] P.J.G. Schwaller, B.J. Tester, D.G. Henshaw, The effects on fan noise of inlet steady flow distortion, 3rd AIAA/CEAS Aeroacoustics Conference (1997) 40–46. https://doi.org/10.2514/6.1997-1590.
[5] P.G.J. Schwaller, N.J. Baker, J.D. Tomlinson, P. Sijtsma, R. Hemmings, Noise validation of model fan rig with engine, Collection of Technical Papers - 12th AIAA/CEAS Aeroacoustics Conference 2 (May) (2006) 1014–1025. https://doi.org/10.2514/6.2006-2479.
[6] Y. Colin, B. Aupoix, J.F. Boussuge, P. Chanez, Numerical simulation and analysis of crosswind inlet flows at low mach numbers, Proceedings of the 8th International Symposium on Experimental and Computational Aerothermodynamics of Internal Flows (2007).
[7] R.J. Astley, R. Sugimoto, G. Gabard, E. Norde, E.J. Grift, M. Bocquier, et al., The effect of steady flow distortion on mode propagation in a turbofan intake, 20th AIAA/CEAS Aeroacoustics Conference (2014) 1–22. https://doi.org/10.2514/6.2014-3113.
[8] J. Winkler, C. Aaron Reimann, R. Reba, J. Gilson, et al., Turbofan inlet distortion noise prediction with a hybrid CFD-CAA approach, 20th AIAA/CEAS Aeroacoustics Conference 3 (June) (2014). https://doi.org/10.2514/6.2014-3102.
[9] M. Doherty, H. Namgoong, Impact of turbofan intake distortion on fan noise propagation and generation, 22nd AIAA/CEAS Aeroacoustics Conference, 2016 (2016) 1–18. https://doi.org/10.2514/6.2016-2841.
[10] M. Daroukh, S. Moreau, N. Gourdain, J.F. Boussuge, C. Sensiau, Influence of distortion on fan tonal noise, 22nd AIAA/CEAS Aeroacoustics Conference, 2016 (2016).

[11] A.G. Prinn, R. Sugimoto, R.J. Jeremy Astley, The effect of steady flow distortion on noise propagation in turbofan intakes, 22nd AIAA/CEAS Aeroacoustics Conference, 2016 (2016) 1–14. https://doi.org/10.2514/6.2016-3028.
[12] J. Winkler, C.A. Reimann, C.D. Gumke, A.A. Ali, R.A. Reba, et al., Inlet and aft tonal noise predictions of a full-scale turbofan engine with bifurcation and inlet distortion, 23rd AIAA/CEAS Aeroacoustics Conference, 2017 (2017) 1–14. https://doi.org/10.2514/6.2017-3034.
[13] M. Daroukh, Effect of distortion on modern turbofan tonal noise, PhD thesis, Université de Toulouse, 2017. https://theses.hal.science/tel-04222919v1/file/DAROUKH_Majd.pdf.
[14] M. Daroukh, S. Moreau, N. Gourdain, J.F. Boussuge, C. Sensiau, et al., Tonal noise prediction of a modern turbofan engine with large upstream and downstream distortion, J. Turbomach. 141 (2) (2019). https://doi.org/10.1115/1.4042163.
[15] M. Daroukh, C. Polacsek, A. Chelius, Shock wave generation and radiation from a turbofan engine under flow distortion, AIAA J. 58 (2) (2020) 787–801. https://doi.org/10.2514/1.J058799.
[16] L. Wu, A.G. Wilson, Fan buzz-saw noise under intake flow distortion: a computational study, 30th AIAA/CEAS Aeroacoustics Conference, 2024 (2024).
[17] C.L. Morfey, M.J. Fisher, Shock-wave radiation from supersonic ducted rotor, Aeronaut. J. 74 (715) (1970) 579–585. https://doi.org/10.1017/s0001924000049095.
[18] A. McAlpine, M.J. Fisher, On the prediction of "buzz-saw" noise in aero-engine inlet ducts, J. Sound Vib. 248 (1) (2001) 123–149. https://doi.org/10.1006/jsvi.2001.3770.
[19] B.S. Stratford, D.R. Newby, A new look at the generation of buzz-saw noise, 44th AIAA Aeroacoustics Conference (1977) 1–23. https://doi.org/10.2514/6.1977-1343.
[20] M. Sanjosé, S. Moreau, M. Pestana, M. Roger, Effect of weak outlet-guide-vane heterogeneity on rotor-stator tonal noise, AIAA J. 55 (10) (2017) 3440–3457. https://doi.org/10.2514/1.J055525.
[21] I. Gonzalez-Martino, D. Casalino, Fan tonal and broadband noise simulations at transonic operating conditions using Lattice-Boltzmann methods, 2018 AIAA/CEAS Aeroacoustics Conference (2018). https://doi.org/10.2514/6.2018-3919.
[22] D. Casalino, A. Hazir, A. Mann, Turbofan broadband noise prediction using the Lattice Boltzmann method, AIAA J. 56 (2) (2018) 609–628. https://doi.org/10.2514/1.J055674.
[23] S. Redonnet, C. Mincu, E. Manoha, Computational aeroacoustics of realistic co-axial engines, 14th AIAA/CEAS Aeroacoustics Conference (2008).
[24] R.J. Astley, R. Sugimoto, P. Mustafi, Computational aero-acoustics for fan duct propagation and radiation. current status and application to turbofan liner optimisation, J. Sound Vib. 330 (16) (2011) 3832–3845. https://doi.org/10.1016/j.jsv.2011.03.022.
[25] B.V. Antwerpen, R. Leneveu, S. Caro, P. Ferrante, New advances in the use of Actran/TM for nacelle simulations, 14th AIAA/CEAS Aeroacoustics Conference (2008). www.fft.be.
[26] M.E. Goldstein, Aeroacoustics, McGraw-Hill, 1976.
[27] Z. Rarata, G. Gabard, R. Sugimoto, J. Coupland, R.J. Astley, H. Namgoong, P.J.G. Schwaller, et al., Integrating CFD source predictions with time-domain CAA for intake fan noise prediction, 20th AIAA/CEAS Aeroacoustics Conference (2014) 1–15. https://doi.org/10.2514/6.2014-2456.
[28] C.K.W. Tam, J.C. Webb, Dispersion-relation-preserving finite difference schemes for computational acoustics, 1993, https://doi.org/10.1006/jcph.1993.1142.
[29] G. Ashcroft, X. Zhang, Optimized prefactored compact schemes, J. Comput. Phys. 190 (2) (2003) 459–477. https://doi.org/10.1016/S0021-9991(03)00293-6.
[30] R. Della Ratta Rinaldi, A. Iob, R. Arina, An efficient discontinuous Galerkin method for aeroacoustic propagation, Int. J. Numer. Methods Fluids 69 (9) (2012) 1473–1495. https://doi.org/10.1002/fld.2647.
[31] M.J. Fisher, B.J. Tester, P.J.G. Schwaller, Supersonic fan tone noise prediction, 4th AIAA/CEAS Aeroacoustics Conference (1998) 290–300. https://doi.org/10.2514/6.1998-2249.
[32] A. McAlpine, M.J. Fisher, On the prediction of "buzz-saw" noise in acoustically lined aero-engine inlet ducts, J. Sound Vib. 265 (1) (2003) 175–200. https://doi.org/10.1016/S0022-460X(02)01446-3.
[33] A. McAlpine, M.J. Fisher, B.J. Tester, "Buzz-saw" noise: a comparison of measurement with prediction, J. Sound Vib. 290 (3-5) (2006) 1202–1233. https://doi.org/10.1016/j.jsv.2005.05.028.
[34] A. McAlpine, M.J. Fisher, B.J. Tester, "Buzz-saw" noise: a comparison of modal measurements with an improved prediction method, J. Sound Vib. 306 (3-5) (2007) 419–443. https://doi.org/10.1016/j.jsv.2007.04.053.
[35] A. McAlpine, P.J.G. Schwaller, M.J. Fisher, B.J. Tester, Buzz-saw noise: prediction of the rotor-alone pressure field, J. Sound Vib. 331 (22) (2012) 4901–4918. https://doi.org/10.1016/j.jsv.2012.06.009.
[36] J.M. Tyler, T.G. Sofrin, Axial Flow Compressor Noise Studies, SAE Technical Paper 620532 (1962). https://doi.org/10.4271/620532.
[37] S.W. Rienstra, Sound transmission in slowly varying circular and annular lined ducts with flow, J. Fluid Mech. 380 (1999) 279-296. https://doi.org/10.1017/S0022112098003607.
[38] A.G. Wilson, Propagation of acoustic perturbations in non-uniform ducts with non-uniform mean flow using eigen analysis in general curvilinear coordinate systems, J. Sound Vib. 443 (2019) 605–636. https://doi.org/10.1016/j.jsv.2018.11.023.
[39] A.G. Wilson, Eigen analysis in general curvilinear coordinates for prediction of noise propagation in aeroengine inlets, 23rd AIAA/CEAS Aeroacoustics Conference (2017). https://doi.org/10.2514/6.2017-3704.
[40] A.G. Wilson, Non-linear acoustic propagation in circumferentially non-uniform mean flow, 25th AIAA/CEAS Aeroacoustics Conference (2019). https://doi.org/10.2514/6.2019-2448.
[41] V. Pagneux, N. Amir, J. Kergomard, A study of wave propagation in varying cross-section waveguides by modal decomposition. Part I. theory and validation, J. Acoust. Soc. Am. 100 (1996) 2034–2048. https://doi.org/10.1121/1.417913.
[42] S. Félix, V. Pagneux, Multimodal analysis of acoustic propagation in three-dimensional bends, Wave Motion 36 (2002) 157–168.
[43] V. Pagneux, Multimodal admittance method in waveguides and singularity behavior at high frequencies, in: J. Comput. Appl. Math., 234, 2010, pp. 1834–1841. https://doi.org/10.1016/j.cam.2009.08.034.
[44] T. Guennoc, J.-B. Doc, S. Félix, Improved multimodal formulation of the wave propagation in a 3D waveguide with varying cross-section and curvature, J. Acoust. Soc. Am. 149 (2021) 476–486. https://doi.org/10.1121/10.0003336.
[45] B. Mangin, M. Daroukh, G. Gabard, Propagation of acoustic waves in ducts with flow using the multimodal formulation, AIAA J. 61 (2023) 2721–2733. https://doi.org/10.2514/1.J062659.
[46] B. Mangin, G. Gabard, M. Daroukh, In-duct flow computation and acoustic propagation using the admittance multimodal formulation, J. Acoust. Soc. Am. 155 (2024) 3461–3474. https://doi.org/10.1121/10.0026091.
[47] J.E. Ffowcs-Williams, D.L. Hawkings, Sound generation by turbulence and surfaces in arbitrary motion, Philosophical Transactions of the Royal Society of London. Series A, Mathematical and Physical Sciences 264 (1969) 321–342.
[48] D.M. Nark, Assessment of radiated fan noise prediction capabilities using static engine test data, in: 17th AIAA/CEAS Aeroacoustics Conference (32nd AIAA Aeroacoustics Conference), American Institute of Aeronautics and Astronautics, 2011. https://doi.org/10.2514/6.2011-2807.
[49] J.A. Hamilton, R.J. Astley, Acoustic propagation on irrotational mean flows using transient finite and infinite elements, AIAA J. 43 (1) (2005) 124–134. https://doi.org/10.2514/1.8306.
[50] S. Caro, P. Ploumhans, X. Gallez, Implementation of Lighthill's acoustic analogy in a finite/infinite elements framework, in: 10th AIAA/CEAS Aeroacoustics Conference, American Institute of Aeronautics and Astronautics, 2004. www.fft.be. https://doi.org/10.2514/6.2004-2891ReadNow.
[51] G. Gabard, R.J. Astley, Theoretical model for sound radiation from annular jet pipes: far- and near-field solutions, J. Fluid Mech. 549 (2006) 315-341. https://doi.org/10.1017/S0022112005008037.
[52] S.W. Rienstra, Fundamentals of duct acoustics, Von Karman Institute Lecture Series (2015) 1–50. https://sjoerdr.win.tue.nl/papers/VKI_Rienstra.pdf.
[53] C.L. Morfey, Acoustic energy in non-uniform flows, J. Sound Vib. 14 (2) (1971) 159–170. https://doi.org/10.1016/0022-460X(71)90381-6.
[54] R. Sugimoto, A.O. James, A. McAlpine, R.J. Astley, CFD/CAA coupling for the prediction of fan tone noise propagation and radiation through a drooped intake, 28th AIAA/CEAS Aeroacoustics Conference, 2022 (2022) 1–15. https://doi.org/10.2514/6.2022-3100.

[55] I.M. Achunche, Acoustic optimisation and prediction of sound propagation in turbofan engine ducts, Ph.D. thesis, University of Southampton, 2010. http://eprints.soton.ac.uk/id/eprint/162395.
[56] P. Mustafi, Improved turbofan intake liner design and optimization, Ph.D. thesis, University of Southampton, 2013. http://eprints.soton.ac.uk/id/eprint/351340.
[57] M. Daroukh, C. Polacsek, T.L. Garrec, J. Thisse, T. Nodé-Langlois, R. Blazquez, Acoustic energy exchange between frequencies during non-Linear propagation of shock waves, 30th AIAA/CEAS Aeroacoustics Conference, 2024 (2024). https://doi.org/10.2514/6.2024-3424ï.
[58] N.C. Ovenden, W. Eversman, S.W. Rienstra, Cut-on cut-off transition in flow ducts: comparing multiple-scales and finite-element solutions, in: Collection of Technical Papers - 10th AIAA/CEAS Aeroacoustics Conference, 2, 2004, pp. 1636–1653. https://doi.org/10.2514/6.2004-2945.
[59] B. Baddour, Duct effects on acoustic source radiation, Ph.D. thesis, University of Southampton, 2023. https://eprints.soton.ac.uk/477328/.